Non-invasive Estimation of Skin Chromophores Using Hyperspectral Imaging

Sriya K. Chakravarty

Thesis submitted to the Faculty of the
Virginia Polytechnic Institute and State University
in partial fulfillment of the requirements for the degree of

Master of Science
in
Mechanical Engineering

Alfred Wicks, Chair
Steve Southward
A. Lynn Abbott

August 1, 2023
Blacksburg, Virginia

Keywords: Hyperspectral Imaging, Kubelka-Munk Theory, Image processing, Non-linear Least Squares, Senstivity Analysis

Non-invasive Estimation of Skin Chromophores Using Hyperspectral Imaging

Sriya K. Chakravarty

(ABSTRACT)

Melanomas account for more than 1.7% of global cancer diagnoses and about 1% of all skin cancer diagnoses in the United States. This type of cancer occurs in the melanin-producing cells in the epidermis and exhibits distinctive variations in melanin and blood concentration values in the form of skin lesions. The current approach for evaluating skin cancer lesions involves visual inspection with a dermatoscope, typically followed by biopsy and histopathological analysis. However, this process, to decrease the risk of misdiagnosis, results in unnecessary biopsies, contributing to the emotional and financial distress of patients. The implementation of a non-invasive imaging technique to aid the analysis of skin lesions in the early stages can potentially mitigate these consequences.

Hyperspectral imaging (HSI) has shown promise as a non-invasive technique to analyze skin lesions. Images taken of human skin using a hyperspectral camera are a result of numerous elements in the skin. Being a turbid, inhomogeneous material, the skin has chromophores and scattering agents, which interact with light and produce characteristic back-scattered energy that can be harnessed and examined with an HSI camera. In this study, a mathematical model of the skin is used to extract meaningful information from the hyperspectral data in the form of melanin concentration, blood volume fraction and blood oxygen saturation in the skin. The human skin is modelled as a bi-layer planar system, whose surface reflectance is theoretically calculated using the Kubelka-Munk theory and absorption laws by Beer and Lambert. Hyperspectral images of the dorsal portion of three volunteer subjects' hands

400 - 1000 nm range, were used to estimate the contributing parameters. The mean and standard deviation of these estimates are reported compared with theoretical values from the literature. The model is also evaluated for its sensitivity with respect to these parameters, and then fitted to measured hyperspectral data of three volunteer subjects in different conditions. The wavelengths and wavelength groups which were identified to result in the maximum change in percentage reflectance calculated from the model were 450 and 660 nm for melanin, 500 - 520 nm and 590 - 625 nm for blood volume fraction and 606, 646 and 750 nm for blood oxygen saturation.

Non-invasive Estimation of Skin Chromophores Using Hyperspectral Imaging

Sriya K. Chakravarty

(GENERAL AUDIENCE ABSTRACT)

Melanoma, the most serious type of skin cancer, develops in the melanin-producing cells in the epidermis. A characteristic marker of skin lesions is the abrupt variations in melanin and blood concentration in areas of the lesion. The present technique to inspect skin cancer lesions involves dermatoscopy, which is a qualitative visual analysis of the lesion's features using a few standardized techniques such as the 7-point checklist and the ABCDE rule. Typically, dermatoscopy is followed by a biopsy and then a histopathological analysis of the biopsy. To reduce the possibility of misdiagnosing actual melanomas, a considerable number of dermoscopically unclear lesions are biopsied, increasing emotional, financial, and medical consequences. A non-invasive imaging technique to analyze skin lesions during the dermoscopic stage can help alleviate some of these consequences.

Hyperspectral imaging (HSI) is a promising methodology to non-invasively analyze skin lesions. Images taken of human skin using a hyperspectral camera are a result of numerous elements in the skin. Being a turbid, inhomogeneous material, the skin has chromophores and scattering agents, which interact with light and produce characteristic back-scattered energy that can be harnessed and analyzed with an HSI camera. In this study, a mathematical model of the skin is used to extract meaningful information from the hyperspectral data in the form of melanin concentration, blood volume fraction and blood oxygen saturation. The mean and standard deviation of these estimates are reported compared with theoretical values from the literature. The model is also evaluated for its sensitivity with respect to these parameters, and then fitted to measured hyperspectral data of six volunteer subjects in different conditions. Wavelengths which capture the most influential changes in the model response are identified to be 450 and 660 nm for melanin, 500 - 520 nm and 590 - 625 nm for blood volume fraction and 606, 646 and 750 nm for blood oxygen saturation.

To Leo

Acknowledgments

As I reflect on the challenging journey of writing this thesis, I cannot help but be grateful to everyone that played a role. The lessons I've learned and the growth I've experienced during this process are immeasurable. This endeavor would not have been possible without the support and guidance of several individuals.

First and foremost, I extend my heartfelt gratitude to my advisor, Dr. Alfred Wicks. His commitment, patience, and profound insights have been pivotal in shaping this thesis. His guidance has not only enriched my academic understanding but also provided emotional support, which was indispensable throughout this journey. I am also grateful to my committee members, Dr. Southward and Dr. Abbott. Their dedicated time and valuable feedback were instrumental in the shaping of my final thesis and enhancing my grasp of the subject matter.

To my parents, a heartfelt thank you. Your belief in me provided the foundation upon which I built this endeavor. My sibling, Neela, deserves special mention for her continuous care, encouragement, and thoughtful check-ins. I am grateful for their presence in my life.

To my dear friends at Virginia Tech – Vignesh, Sharifa, and Bhavi – thank you for your companionship and reassurances, and for making the challenges of this endeavor feel lighter. A heartfelt acknowledgment also goes to the members of the Applied Autonomy and Mechatronics Research Lab and the AutoDrive Team, for providing an intellectually engaging and supportive environment during my master's study. I extend my gratitude to all those who have touched this journey. Thank you everyone for being a part of this chapter in my life.

Contents

List of Figures

List of Tables

Chapter 1

Introduction

The healthcare industry is constantly searching for non-invasive diagnostic techniques that provide high-reliability data to confirm diagnoses. Passive techniques like the simple stethoscope or the electrocardiogram "listen" for indicators related to conditions of the heart and lungs, with no input from the measuring device. In contrast, active sensors, such as ultrasound machines, provide known acoustic energy to the region of interest and measure the reflected response. With the advancement in measurement technology, the different regions of the electromagnetic spectrum have been leveraged to obtain health information from patients. Low-energy radio ways coupled with strong magnetic fields are used in Magnetic Resonance Imaging (MRI) machines [10] to form images of anatomy in a matter of a few minutes. Medical imaging carried out by X-ray [11] machines and CT (Computed Tomography) [12] scanners harnesses higher energy regions of the electromagnetic spectrum.

Medical imaging devices operate on the fundamental principle that biological and pathological tissues interact significantly with incident electromagnetic waves. This results in unique spectral signatures that depend on the scattering and absorption properties of the tissue's molecular components [13]. Typically, incident electromagnetic energy is absorbed or scattered by the tissue through various processes, depending on the wavelength of incident energy and the dimension of the constituent particles. Most tissues are weak absorbers and permit light penetration within the therapeutic window ranging from 600 to 1300 nm [14].

In general, anatomical structures do not require contrast to be visible by medical imaging devices. Incident electromagnetic radiation can cause transitions between two energy levels of a biological molecule that are well-defined at specific wavelengths, as defined by Planck's quantum theory. This energy change can be captured by a medical imaging device. The term 'chromophore' refers to the part of the molecule that gives rise to the transition of interest, and ultimately the color of the molecule [15]. In some cases, a specific wavelength can elicit a florescent response. This kind of response involves the absorption of light at a certain wavelength, followed by the emission of light at another wavelength a few nanoseconds later. However, in the absence of any such response, exogenous contrasts can be employed to block the incident energy, thereby highlighting the anatomical structures of interest.

Measurements based on light have been a standard approach in the military and healthcare industry for decades. Applications vary from range estimation using LIDARs (Light Detection and Ranging devices), isolation of camouflaged humans and foliage using multispectral cameras, to medical fluoroscopy and CT scans. In the last few years, with the advent of the COVID-19 pandemic, pulse oximetry has become a commonly used method for bedside health monitoring. Pulse oximetry is a non-invasive, light-based approach that measures arterial blood oxygen levels and pulse wave activity [16]. In pulse oximetry, lights of known wavelengths are directed into the skin and the reflected light is analyzed to make measurements. Pulse oximetry is now the minimum standard in intra-operative monitoring by multiple federal and world medical organizations. Besides hospital-grade pulse oximeters, smaller and portable consumer-grade models have become increasingly prevalent in sports, private aviation, and mountain climbing to estimate pulse rate activity as well as stress levels.

Hyperspectral imaging can be considered an extension of pulse-oximetry, which is essentially a form of spectroscopy. Changes in the intensity of light of known wavelength indicate a physical phenomenon that can be measured. Hyperspectral imaging cameras are sensitive to several continuous wavelengths and form an image of the region that it scans [17]. While this approach may be misunderstood to be passive, the camera cannot detect back-scattered energy until there is some known input illumination on the area of interest. This makes it an active sensing method.

This chapter provides a broad overview of the key topics covered and the motivation of this thesis, including hyperspectral imaging, skin cancer, specifically melanomas, and the intersection of these two areas. This chapter aims to present these complex concepts in a clear and understandable manner for the reader. It begins by tracing the history of hyperspectral imaging and outlining its primary applications in recent decades. The subsequent section introduces the topic of skin cancer and highlights its severity, concerning recent statistics. The chapter then delves into the overlap between these two fields, exploring how hyperspectral imaging can be used to detect and diagnose skin cancer. The chapter concludes with a summary of the main themes covered in the following chapters of the thesis.

1.1 Hyperspectral Imaging

Hyperspectral imaging (HSI) is a non-invasive, contactless technique that captures and analyzes surface information across a continuous range of the electromagnetic spectrum [17]. HSI combines imaging and spectroscopy in one system and allows the collection of spatial and spectral data. The human eye has receptors only in three colors or wavelengths, namely, red, blue, and green in the visible region of the electromagnetic spectrum (400 - 700 nm) [18]. In contrast, a hyperspectral camera captures and measures a continuous spectrum of reflected light from a scene, covering a calibrated wavelength range. HSI cameras can be sensitive to wavelengths ranging from 300 to 2500 nm, which encompasses the ultraviolet (UV), visible (VIS), and near-infrared (NIR) regions. It allows for the detection of materials that are not visible to the human eye, and it can provide information about the chemical composition of an object or scene.

The first hyperspectral imaging instrument was developed in the 1980s at NASA's Jet Propulsion Laboratory for airborne remote sensing. The instrument was called AVIRIS (Airborne Visible Infra-Red Imaging Spectrometer) and can cover wavelengths ranging from 400 nm to 2500 nm with a spectral resolution of 10nm [19, 20]. The instrument is still used for quantitative measurement and detection of surface and atmospheric constituents present on the earth. With the increase in computing power, hyperspectral imaging finds itself at the forefront of many food and agricultural technologies as well [21]. Online inspection of food quality, safety, and pathogen detection in meat products [22], fish [23], fruits and vegetables [24] and grain [25] has been extensively researched in the past couple of decades [26].

Hyperspectral imaging has gained significant attention in the medical field due to its ability to provide detailed and precise information about the spectral characteristics of tissues and organs. Furthermore, HSI enables non-invasive and real-time in-vivo analysis of unhealthy tissue, addressing the need to avoid costly and emotionally taxing procedures [27]. Monitoring oxygenation and creating oxygenation maps for different targeted regions in the body can help aid the diagnosis of diseases related to arterial occlusions such as peripheral artery disease (PAD) [28], diabetic foot [29], and various cancers [30]. For highly sensitive and delicate parts of the body like the retina, combining hyperspectral imaging with a standard fundus camera can be extremely beneficial. Retinal oxygenation monitoring with HSI cameras can be used for early diagnosis and to determine the efficacy of therapy [31]. Studies have shown that these oxygenation maps can become extremely detailed and have the ability to depict the networking structures inside cancer lesions and biopsies as well [32]. In general, hyperspectral has been identified as a powerful technique to help distinguish cancerous and unhealthy tissue from healthy tissue. This could be during in-vivo or in-vitro examination, or in the surgical field, where getting clear margins and excising the entire tumor is of primary importance.

1.2 Motivation

Skin cancer is the uncontrolled growth of abnormal cells in the epidermis due to unrepaired DNA damage, which in turn triggers mutations. The main types of skin cancers in human beings include basal cell carcinomas (BCC), squamous cell carcinomas (SCC), melanomas, and Markel cell carcinomas (MCC). Melanomas are specifically related to the overgrowth of melanocytes, the cells in the skin that give it color [33]. While melanomas are the most curable of the four types of skin cancers, invasive melanomas are projected to be the fifth most commonly diagnosed cancer in the United States.

Studies have shown that early detection of melanomas greatly increases the chances of successful treatment [34]. However, if left untreated and advanced, they can metastasize rapidly to the lymph nodes and internal organs, ultimately leading to death. In the United States, more than 9500 people are diagnosed with skin cancer every day, and at least two people die of the disease every hour [35]. Out of these, there has been an estimated 27% increase in the number of invasive melanomas in the past decade. A large number of studies indicate a direct correlation between malignant melanomas, and genetic and personal characteristics, as well as a person's exposure to UV radiation [36].

Although Caucasians are generally at a higher risk of developing skin cancers, including melanomas and non-melanomas, individuals with darker skin tones are often diagnosed at later stages. This makes treatment more challenging for people of color. In fact, the five-year survival rate for patients of color is only 70%, in stark contrast to the rate for white patients, which is around 94% with a survival rate of over 99% when diagnosed early [35].

The present methodology to diagnose skin lesions involves visual inspection as well as using a dermatoscope, a device that helps enhance a dermatologist's view of the skin [37]. Even though a dermatoscope has proven to be more effective than visual inspection, a large number of skin lesions are biopsied to confirm a diagnosis. This is an attempt to mitigate misdiagnosis. However, this conservative approach has led to a trend of over-prescribing invasive biopsies. Patients spend time, money, and energy on unnecessary procedures that are emotionally and physically toiling. A study conducted by the University of Washington indicates that dermatopathologists agree with the concern of overdiagnosis [38]. Furthermore, despite the existence of algorithms such as the 7-point checklist and the ABCDE method that aid dermatologists while examining a skin lesion, small changes in skin lesions challenge even expert dermatologists [39]. This creates a need for a standardized instrument to help diagnose skin cancer or ascertain a requirement for a biopsy.

In light of this requirement, a number of research groups have recently come up with possible solutions. In recent decades, hyperspectral imaging has emerged as a novel approach for the detection and classification of skin cancer. As mentioned earlier, biomarkers such as oxygenation maps and water retention models using data in the IR and UV ranges can be used to enhance skin lesion analysis [40]. These models can be leveraged to train artificial intelligence algorithms that can distinguish between benign moles and malignant melanomas.

The primary aim of this thesis is to validate a numerical model for the human skin as a function of its constituent chromophores, to prove that it can be effectively used to discern variations between healthy and unhealthy skin. Additionally, identifying wavelengths that are most responsive to variations in different components in the skin can be a powerful tool in making the model and the hyperspectral acquisition system more efficient. It is also extremely important for the model to be inclusive of people of color, and be able to accurately capture characteristics of skin for individuals with higher melanin content.

1.3 Chapter-wise breakdown

Chapter 2 provides a detailed background on the key topics covered in this thesis, including hyperspectral imaging (HSI) and its application on human skin. The first section of the chapter introduces the procedure involved in standard digital imaging, multispectral imaging, and hyperspectral imaging. Special emphasis on the imaging process involved in HSI is given. The following section focuses on a review of literature of the original and recent advances made in the application of HSI of human skin. The current state-of-the-art technology in HSI-assisted diagnostics for skin cancer is also presented.

Chapter 3 focuses on the experimental portion of this research study. Specifications of the HSI camera used in this study are presented. The requirement for known input illumination is highlighted and the lighting system used to perform experiments is presented. The basics of a typical image acquisition sequence are explained, illustrating the meaning of white references and dark frames in spectroscopy. Calibration experiments focus on characterization of the illumination system, identifying regions of interest and adjusting the lens. An innovative model to estimate a low-cost white reference at the most suitable exposure time is explained and corroborated with appropriate findings.

In Chapter 4, the concept of hyperspectral imaging is presented from a physics perspective. The theory behind a surface's interaction with incident electromagnetic energy is explained, including absorption bands, Rayleigh and Mei scattering and transmission effects and fluorescence in materials. The Kubelka-Munk theory for the optics in paint layers and the Beer-Lambert-Bouguer law is also explained, in the context of mathematically modelling human skin. Finally, the complete numerical simulation of the reflectance on the surface of the skin used in this thesis is defined. The objective function relating the numerical model to the measured data outlined in Chapter 3 is presented, with a brief description of the gradient based optimization method used to minimize the objective function.

The results from the experimental and numerical sections are discussed in Chapter 5. The images obtained by the hyperspectral camera are displayed, and important features of the images are highlighted. Hyperspectral images of two sets of imaging trials are displayed, with important features highlighted in each image. The images are followed by a sensitivity analysis of the mathematical model developed in Chapter 4. This analysis results in wavelengths in the visible and near-infrared regions which are most sensitive to changes in chromophores and scattering agents in the skin. Finally, the outcomes of the minimization function are presented, along with appropriate discussions and conclusions.

Chapter 6 provides an insightful summary of the findings from this thesis and suggests possible areas of future research. The chapter also reflects on the limitations of this research effort, including that of the model and the hyperspectral camera used. The future work section provides recommendations for addressing these gaps through AI-assisted models and modifications to hyperspectral imaging set-up.

Chapter 2

Background

This chapter introduces concepts of standard imaging, hyperspectral imaging (HSI) and processing of data obtained from HSI in detail. It also gives an overview of some camera configurations used in HSI. Finally, the chapter delves into the advancements in the hyperspectral imaging of biological tissue and human skin.

2.1 Hyperspectral Imaging

Imaging has revolutionized the scientific world and the way humans capture and interpret their surroundings. Cameras, invented as devices designed to preserve moments in time, have gone well beyond their artistic application and have been used to quantitatively describe the world. In the digital age, the advent of imaging sensors such as charged-coupled devices (CCDs) and complementary metal-oxide-semiconductors (CMOS) sensors have altered the ability to process visual data. These devices convert light intensities into precise electrical signals, that can be analyzed using analysis techniques. Digital imaging has now contributed to countless fields such as medical diagnostics, remote sensing, autonomous vehicles, and human-assistive technology by aiding the storage and processing of data conveniently. Most often taken for granted as a standard feature in smartphones, cameras are indispensable tools that overcome the limitations of plain text.

A modern-day digital image is a two-dimensional (2-D) matrix of numeric values that displays intensity or brightness information in a particular wavelength or color. In other words, an image can be considered as a X × Y matrix, whose cells are called pixels. The size and resolution of the image is defined by the imaging sensor used [41]. Advancement in semiconductor technology makes it possible for images to have resolutions going beyond 100 million pixels. Each pixel or a group of pixels corresponds to photoreceptors embedded in the imaging sensor. Photoreceptors in imaging sensors could be semiconductor capacitors or photodiodes in conjunction with MOSFETs depending on the application. The human eye can also be considered as an imaging sensor, containing roughly 576 million pixels [42]. The photoreceptors in this case, are in the form of rods and cones in the retina, which are sensitive to different ranges of the electromagnetic spectrum, as shown in Figure 2.1 [43]. The peaks in the aforementioned figure indicate wavelengths at which the photoreceptors are most likely to absorb photons. The figures shows the three types of cones, usually named S, M and L for small, medium and large wavelengths respectively. The regions of overlap in the sensitivity spectrums allow the eyes to perceive more than just in peaks of red, blue, and green (RGB).

The photoreceptors in an imaging sensor use filters to create light sensitivity spectrums like those of rods and cones, since photoreceptors capture little to no wavelength information [44]. Each pixel contains a numerical value indicating brightness or intensity received by the sensor in a particular wavelength. This value is a function of the analog-to-digital converter (ADC) resolution of the processing chip in a camera. For a high-quality camera with an ADC resolution of 12, the brightest white in a scene is denoted by the highest value 2^{12-1} (4095) and the darkest spot is 0. To depict a scene in color, 2-D images are taken at several wavelengths or bands and then combined. The 2-D digital images are analogous to stacked slides, creating a composite color image when observed from a top-down perspective. A

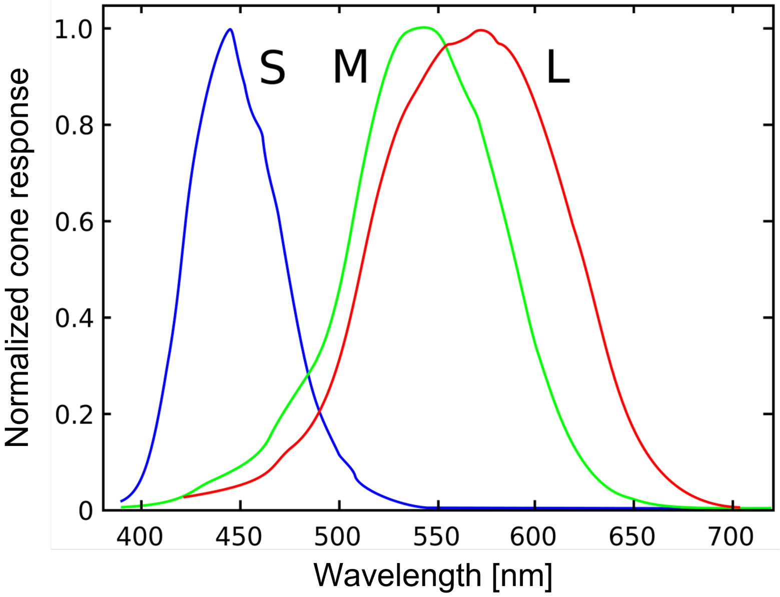

Figure 2.1: Senstivity spectrum of S, M and L cones in the human eye, referring to short, medium and long wavelength sensitive cells. The peaks of the three types are at 420 nm, 530 nm and 560 nm, with the short-wavelength sensitive cones being the least common [1].

schematic depiction of such an image is shown in the Figure 2.2. The color image on the far left is a composite of the three gray-scale images containing intensity information in the red, green and blue wavelengths. A similar process occurs in the human eye – the wavelength sensitive rods and cones capture images in 3 major wavelengths (RGB) and the brain processes these as colorful images of a scene [41].

By increasing the number of wavelengths that the images are taken, the amount of information captured from a scene and depicted as an image can be increased. This type of imaging is termed multi-spectral imaging. In multi-spectral imaging, 2-D images at numerous discrete bands or wavelengths are captured and combined to form a 3-D image or a data-cube with two spatial dimensions and one spectral dimension ($X \times Y \times N$). Typically, the number of spectral band lies between 3 to 15 for multi-spectral images. For the images to be interpretable by humans, these images are depicted in false color using only three out of N wavelengths. When the discrete bands are dense enough that they appear to be

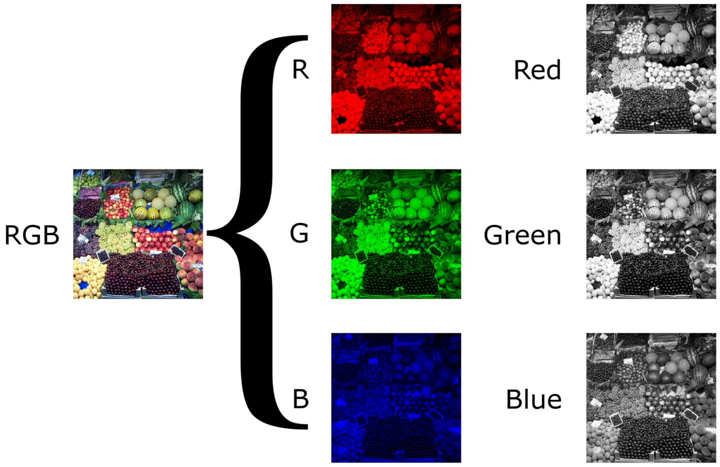

Figure 2.2: Schematic of three 2-D images in red, blue and green wavelengths combined to form color images. The 2-D image is the intensity reflected back from the scene at a particular wavelength [2].

continuous, it is called Hyperspectral imaging (HSI). Usually, the number of spectral bands in a hyperspectral camera are more than 100, with the interval between adjacent wavelength bands going as low as 2 nm. The continuous nature of the spectral dimension enables the representation of a pixel as a spectrum. The spectrums are similar to those obtained from a spectrometer; an optical instrument used to measure continuous spectral components from a physical phenomenon. Hyperspectral pixels depicted as a spectrum can be manipulated using spectral analysis methods just like those from spectrometers [41]. The AVIRIS remote sensing instrument at the Jet Propulsion Laboratory is one of the most exceptional hyperspectral sensors in the industry, with a spectral covereage from 400 to 2450 nm, and a spectral resolution of 10 nm [45]. An example of a commercial hyperspectral cameras in the visible and near-infrared regions (VNIR) is the line-scanning xiSPEC2 by XIMEA [46], which has a spectral range of 470 - 900 nm and 150 bands.

A characteristic capability of a hyperspectral camera is the ability to capture spatial (X, Y) and spectral (λ) data in one, combined data format. This is carried out in a number of ways.

There are typically three configurations through which a hyperspectral camera captures spatial information. These are called whiskbroom, push-broom and snap-shot configurations. The whiskbroom or spotlight configuration involves point scanning, where the reflected light from a scene is captured one pixel at a time. This configuration results in high resolution images but is extremely time-consuming and expensive. A more time efficient and economical option is the push-broom structure where the sensor detects the scene line by line. Hence, this configuration is also known as along-track scanner or line scanner [41]. Finally, the configuration with the shortest acquisition time is the snapshot type. The entire 3-D data cube with spatial and spectral data is captured in one snapshot of the scene. The excessive cost and manufacturing limitations associated with snapshot hyperspectral cameras make them more suitable for research than commercial applications [47].

With every incidence of spatial acquisition, the spectral breakup of that region must be stored. To obtain spectral information, the reflected light from the target scene is split into its constituent spectral components using a dispersing optical instrument such as a diffraction grating, or a prism present in the camera housing. These diffracted rays fall on the detector, which has bandpass filters that correspond to the spectral resolution of the camera. Two schematic diagrams explaining this process are shown in Figure 2.3. Since hyperspectral imaging originated in the realm of remote sensing, the hyperspectral imaging sensor in satellites captures all reflected light from a target scene that is illuminated by the sun. However, a typical laboratory or industry spectrometer requires an illumination source that has energy across the sensitivity spectrum of the detector.

The human eye, spectrometers and hyperspectral cameras have another trait in common – since they are sensitive to the reflected light from a scene, they inherently also indicate which regions of the electromagnetic spectrum are most absorbed by elements in the scene.

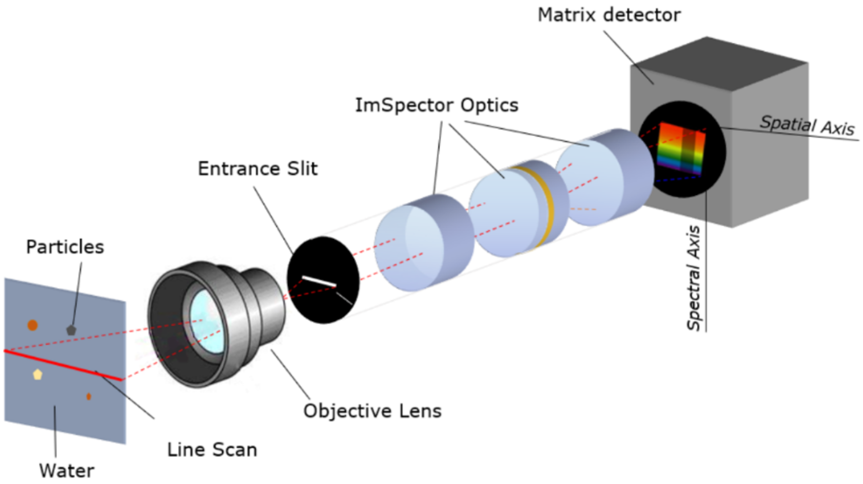

Figure 2.3: ImSpector® (Specim, Fl) imaging spectograph anatomy [3]. Light reflected back from a scene passes through a lens and then a narrow entrance slit. The line of light energy is dispersed by a diffraction grating or dispersive element, and projected onto an imaging sensor that has wavelength filters on it. This is stacked together, as the camera scans a scene to for a hyperspectral image.

This ability of a hyperspectral camera can be leveraged to image various multi-component scenes. In remote sensing, this would involve a landscape being imaged from a satellite like a Landsat. In the context of biomedical imaging, a chosen region of the body or a biopsied tissue is observed by a laboratory hyperspectral camera and probed for the various components in the specimen.

Ideally, each pixel in a hyperspectral image consists of only one constituent material and can be characterized by the material's spectral properties. This is possible when the targets are big enough to cover the entire pixel, as in the case of industrial settings where hyperspectral cameras are used to classify different polymers and plastics. Such pixels encompassing only one material are known as pure pixels. When targets in a scene are magnitudes smaller than the spatial sampling resolution, such as in remote sensing and biomedical imaging, multiple targets are embedded into a single pixel. These constituent substances cannot be resolved solely by their spectral properties and must undergo considerable signal processing and unmixing to be effectively separated out [17]. In the case of biomedical imaging, there has been ample research in using a physics-based model to aid the spectral unmixing of a biological tissue's constituents. Ranging from intro-operative to superficial imaging of the skin, hyperspectral imaging has proven to be a valuable tool to facilitate non-invasive diagnoses in the biomedical field.

2.2 Hyperspectral Imaging of Human skin

Imaging has played a significant role in dermatology and skin research over the past few decades. Clinicians, scientists, and dermatologists have used many imaging techniques in their routine practice to aid diagnoses, monitor treatment effectiveness and disease progression. The dermatoscope, a standard imaging tool used in dermatology checkups, is a handheld device capable of magnifying the area of interest up to 40 times and illuminating it with LED lights [48]. Advanced versions of the dermatoscope offer a unique feature using LEDs of varying colors and polarization, enhancing the visualization of pigmented structures within skin lesions [49]. Despite these technological advancements, the analysis of dermatoscope images still relies on the expertise of the dermatologist conducting the checkup, leading to considerable variability in diagnoses due to differing levels of experience [39]. Nevertheless, when compared to naked eye examinations, the dermatoscope demonstrates a significant improvement in detecting melanomas and accurately identifying non-melanomas as benign cases [50]. Furthermore, over the past 20 years, with the intervention of cutaneous and subcutaneous imaging, dermatology is not only limited to simple visual and touch examinations. Spectrophotometry or spectral imaging through multispectral and hyperspectral imaging has gained significant ground as an assistive tool during dermatological assessment.

Human skin consists of many chromophores, predominantly blood, melanin, bilirubin, and beta-carotene. Blood itself has unique absorption spectrums for oxygenated and deoxygenated hemoglobin, a crucial distinction for the implementation of pulse-oximetry. In addition to these chromophores, the skin is a highly effective scattering agent consisting of a series of inhomogeneous layers; the stratus corneum, the viable epidermis and the dermis [51]. When the skin is illuminated with a source, the reflected light is scattered at many angles, resulting in diffuse reflections. This diffuse reflection is due to the plethora of scattering centers present under the surface of the skin and is what is captured by the hyperspectral camera as diffuse reflectance. The measured diffuse reflectance is a mixture of countless signals that arise from scattering, absorption, and reflection processes inside the skin. The 3D data cube consists almost entirely of mixed pixels due to the irregular distribution of chromophores which must be spectrally unmixed.

Spectral unmixing has been a fascinating topic for many researchers since the inception of hyperspectral imaging [17]. Typically, spectral signatures of constituent materials in remote sensing are unmixed using techniques such as pixel purity index [52], N-FINDR [53], independent component analysis (ICA) and principal component analysis (PCA) algorithms[17]. Most of these algorithms assume pure pixels exist in the scene and use projections onto these assumed pure pixel spectrums to decouple signals. However, such an assumption does not hold credence in the case of human skin as there are no pure pixels present in diffuse reflectance spectra. Thus, researchers have leaned towards using multi-layer analytical models to extract and map skin in recent times.

Initial studies by Nagaoka et al. [54] focused on extracting melanin (M) and erythema (E) indices from diffuse reflectance spectra obtained over time. A dip in reflectance is observed between wavelengths 500 nm and 600 nm, which represents scattering and absorption by blood hemoglobin. Reflectance here refers to how much of the input energy is reflected back, as acquired from a spectrometer. The study hypothesizes that changes in this dip can be leveraged to calculate blood circulation, while other regions of the spectrum can be fit to obtain pigmentation values. The results were justified using an occluded arm as a reference, and monitoring changes as the occlusion was introduced and removed. The results obtained from this study are corroborated by those obtained from Dolotov et al. [55] , where a similar approach to calculate M and E was applied to only three specific wavelengths, 560, 650 and 710 nm.

Subsequently, several research groups explored implementing inverse models that use radiative transfer equations (RTEs) on measured diffuse reflectance spectra to find skin chromophores. An approximation to the RTEs using Kubelka-Munk Theory for the optics in paint layers has been widely used to describe human skin [56]. The skin is usually modelled as a plane-parallel multi-layer slab with light travelling in one dimension through the thickness of the slab. Preliminary studies that model human skin do not measure diffuse reflectance to validate their methodologies [57]. They in turn use GPU-accelerated Monte Carlo simulations to obtain the design space of diffuse reflectance of human skin and inversely solve for various skin chromophores [58]. In this regard, Yudovsky and Pilon [59] proposed an appropriate analytical formulation that builds on RTEs and the Kubelka-Munk theory. Wavelengths are limited to the visible region, and results show a relative error of less than 8%.

This model was further adapted to fit diffuse reflectance spectra obtained from hyperspectral images [60]. The same group applied the model to detect ulcerations early in the feet of people diagnosed with diabetes. Comparison of oxygenation maps under the foot before and after ulcerations revealed predictability in the behavior and progression of the lesions [61]. A simpler application is comparing reflectance spectra of skin before and after occlusions, as done by Zherebtsov et al. [57]. Accurate estimation of oxygenation maps, melanin maps and skin thickness for human skin and bio-tissue phantoms mimicking human skin were obtained.

In addition to physics-based models, research studies by Gevaux et al. [62] and Hosking et al. [63] augment their estimations with machine learning techniques. Specifically, Gevaux et al. [62] used a multi-layered perceptron, that uses reflectance at 31 wavelengths to predict 4 output signals corresponding to oxygen rate, blood volume fraction, melanin concentration and epidermal thickness. These values are compared with outputs from a simple optimization algorithm that minimizes the distance between measured and calculated reflectance from a formulation similar to Zherebtsov et al. [57] that uses the Kubelka-Munk theory. While the work presented in this paper is impressive, the validation of results is weak, and the model does not consider any light transport mechanisms.

Hosking et al. [63] and [32] on the other hand, published a functional prototype of a device in 2019 that can be used for the early detection of melanomas and to indicate a requirement for biopsy. This device was called mAID, the melanoma advanced imaging dermatoscope. The device uses a hyperspectral camera with a spectral range of 350 - 950 nm and returns a Q-score identifying the probability of melanoma for each lesion that is imaged ($0 =$ common mole, $1 =$ melanoma). The device was designed with previous melanoma detection devices on the market in mind. These include MelaFind, and the SIAScope, which have been argued to be impractical or unhelpful in clinical situations, either due to always recommending biopsy or not improving diagnostic abilities of dermatologists. Fifty diagnostic melanoma imaging biomarkers (MIBs) are determined for each image and used to obtain a diagnostic Q-score for the probability of melanoma. Number of colors in the lesion, border and brightness of the lesion, symmetry and organization of pigmented patterns, networks and substructures over the different wavelengths are a few MIBs used in the study. The MIBs were fed into 13 machine learning algorithms to evaluate the probability of melanomas in each, and then the median of all the results was calculated as the Q-score. Initial results show promise in diagnosing melanomas using hyperspectral imaging in a clinical setting and the device is in the early stages of a clinical trial.

2.3 Summary

This chapter goes over the background of hyperspectral imaging (HSI) and its application in the healthcare industry. To elucidate the functioning of hyperspectral imaging, an analogy is drawn between the sensor used in hyperspectral imaging and the human eye. The data format and dimension obtained from a HSI camera is explained in detail. It is evident that HSI provides enormous amounts of information about a scene. Various image processing and spectral analysis techniques have been proposed to tackle the problem of extracting meaningful insights from the data, including physics-based models and black-box machine learning algorithms. In the health-care industry, the latter solution faces skepticism by medical professionals, owing to the lack of transparency and interpretability. However, certain foundational physics-based frameworks to model biological tissues have been established. A review of the existing literature reveals a need to investigate how these models are influenced by individual variables. Additionally, the importance of characterizing biomarkers is apparent, especially for the model to have diagnostic value.

Chapter 3

Technology

Hyperspectral cameras are powerful instruments for capturing detailed spectral information from a scene. For remote sensing, these cameras are installed in satellites that fly over large regions of the Earth and capture reflected energy from its surface, aiding in environmental monitoring, land classification and resource exploration. Multispectral and hyperspectral cameras have also been installed in exploratory missions to other planets for the same applications. In laboratory settings, hyperspectral camera set-ups contain a combination of an illumination system and a mechanical system to enable scanning the region of interest (ROI). In this chapter, the components and calibration of the laboratory based hyperspectral imaging set-up used in this study are discussed in detail.

3.1 Hyperspectral Camera

The hyperspectral camera employed in this thesis is the push-broom PFD4K-65-V10E (2015) hyperspectral camera from Specim, Spectral Imaging LTD (Finland). This camera uses a CCD imaging sensor, the Imperx 2M30, with an active image area of 11.84 × 8.88 mm and a diffraction grating with a slit size of 30 µm × 8.98 nm. It is mounted with a C-mount lens of focal length 23 mm and a maximum aperture of f/1.4. Additionally, the camera has a spectral resolution of 2.73 nm, and a nominal spectral range of 400 – 1000 nm, which is called the Visual and Near-infrared regions (VNIR). The camera is also equipped with a

12-bit ADC, and acquires signals in the range [0, 4095]. The data-cube obtained from the camera has dimensions that follow the X × Y ×λ convention, where Y is a fixed at 1600 pixels, λ refers to the 840 wavelengths captured, and X is the variable spatial dimension that depends on the distance the camera traverses in one push-broom sweep. The number of pixels captured in the Y-dimension is dictated by the fixed length of the diffraction slit and the pixel size in the imaging sensor. A schematic of this capability is displayed in Figure 3.1, where the field of view (FOV) in the Y-direction is depicted to be fixed, and the light coming into the slit is dispersed into the spectral plane and onto the imaging sensor. The camera typically produces a hyperspectral image data-cube with dimensions 1600 × 1200 × 840 when panned a full 180 degrees.

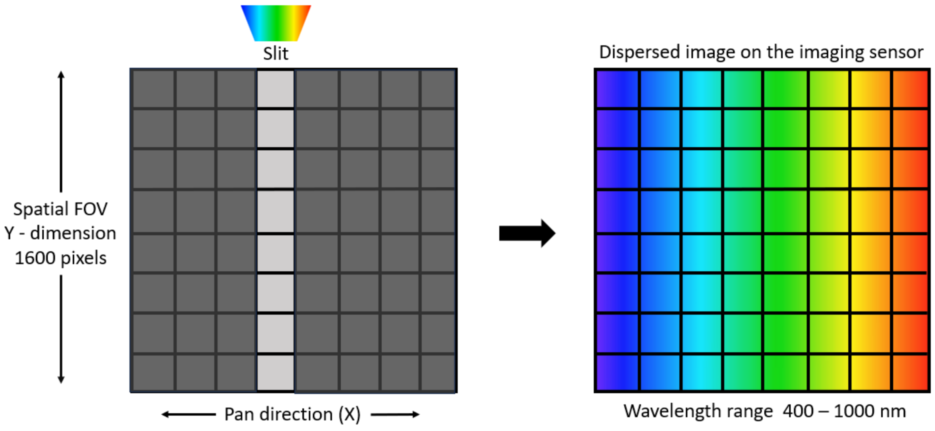

Figure 3.1: Schematic depicting dispersion of light onto imaging sensor in Hyperspectral Camera. Reflected light enters the slit of fixed length, and is dispersed onto the imaging sensor. The spatial field of view (FOV) in the Y - dimension is fixed at 1600 pixes, and is determined by the dimensions of the imaging sensor and the entrance slit.

The hyperspectral camera was mounted onto a pan-tilt utility (PTU) provided by the manufacturer to enable the push-broom functionality of the camera. The PTU was controlled using a user-interface on a computer, and the entire set-up was mounted onto a cart – termed the Hyperspectral Imaging Cart. In order to image surfaces of the skin, 80-20s aluminium bars were used to alter the set-up so that the camera points downwards. Due to the downward pointing mount, the distance to the surface or object to be imaged remains constant, making it convenient to focus the lens and determine the panning distance required for imaging skin sections. To localize the ROI for imaging, an aluminum sheet was cut into a rectangle, with a concentric rectangular window of size 25.4 × 50.8 mm in the middle. A picture of the window is shown in Figure 3.2a. As seen in the image, all sharp edges were filed and taped off for safety. To image a particular region on the body such as the dorsal portion of the hand, the user must place their hand beneath the aluminum sheet, while the camera pans the specified X-distance. Figure 3.2b depicts the Hyperspectral Imaging cart with the downward point camera.

(a) Window marking region of interest (ROI)

(b) Hyperspectral imaging cart

Figure 3.2: Hyperspectral imaging set-up. The window marking the region of interest is cut-out on an aluminium sheet and taped off. The diffused light source is held by a 3-D printed fixture. The entire setup consists of a computer that is connected to the Pan-Tilt Utility and Hyperspectral camera, a power supply connected to the illumination system and the window marking the region of interest placed under the camera.

3.2 Illumination source

For any camera to capture a scene, it is obvious a source of input light is required. However, in the case of a hyperspectral camera, the output image captures a continuous spectrum from a scene and therefore the source of illumination must also be continuous in terms of wavelength. In the case of remote sensing, the sun serves as the continuous illumination source, spanning a wavelength range of 100 nm to about 1 mm (1,000,000 nm). It has a radiation comparable to that of a black body of about 5900 K, as shown in Figure 3.3, where it is compared with the emission spectrum after atmospheric absorption. Similarly, in a laboratory set-up, a source like the sun's emission spectrum with even energy across most wavelengths is preferred. Halogen lights are the most common and cost-effective light source for hyperspectral imaging, due to their continuous emission spectrum. As shown in Figure 3.4, a comparison between the emission spectrum of sunlight, incandescent, fluorescent and LED lights. Keeping in mind that halogen lights are a more efficient and whiter version of incandescent lights, it is evident that that halogen lights provide the most uniform illumination for a laboratory setting. In this study, a 12-V, 100-watt tungsten-halogen metal reflector lamp is used, being the most common light sources currently used in microscopes and other research-level applications.

Tungsten-halogen incandescent lamps operate as thermal radiators – the output light intensity is dependent on the temperature reached by the filament. A disadvantage of this is at higher wavelengths, most of the energy emitted by these lamps is dissipated as heat. The emission spectrum of the halogen light used in this study is displayed in Figure 3.5, which is similar to those observed in reference literature [64]. The plot combines readings from two spectrometers in the visible (335 – 820 nm) and near-infrared regions (630 – 1120 nm). The spectrometers have an ADC resolution of 14, making it more sensitive than the hyperspectral camera used in this study. In the plot, a gamma distribution curve envelopes the emission spectrum to highlight the overarching behavior of the halogen light spectrum.

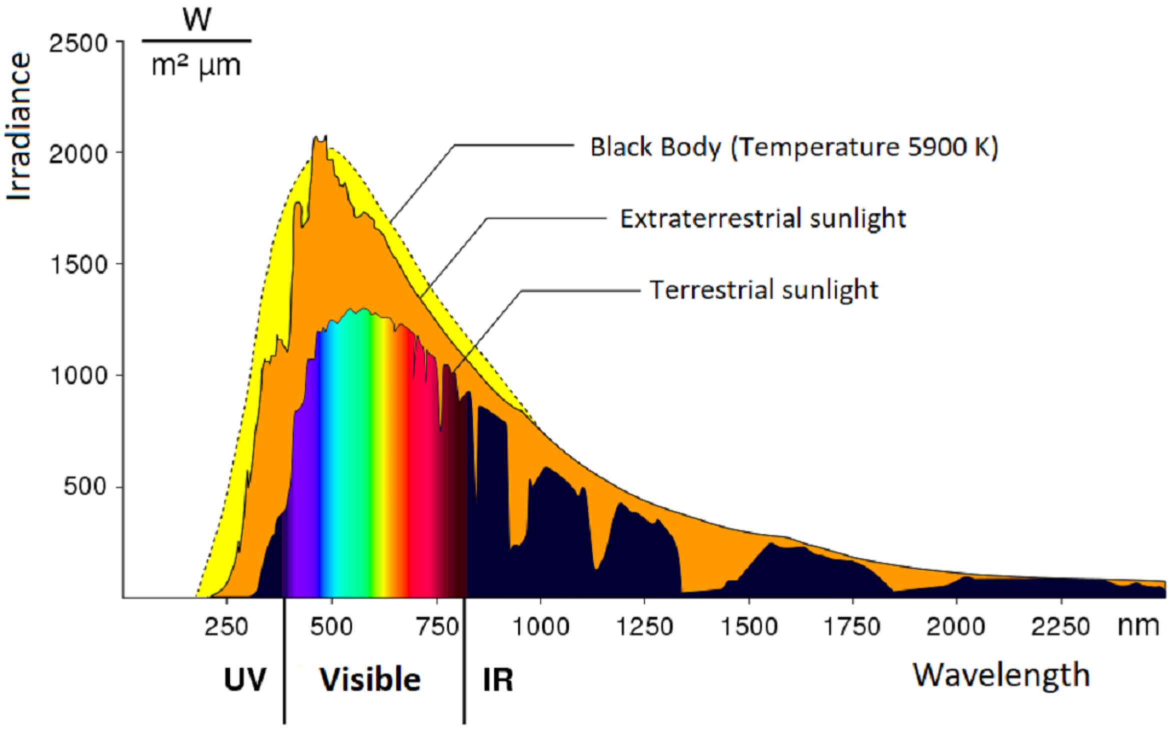

Figure 3.3: Comparison of spectral irradiance of a blackbody of temperature 5900 K (yellow) to the solar emission spectrum before (orange) and after (rainbow) it enter's the earth's atmosphere. The drops in irradiance value are associated with energy absorption by molecules in the atmosphere. [4]

Only about 15% of the entire emitted energy falls within the visible region (400 – 700 nm), with the majority energy lying in the infrared and near-infrared regions.

Throughout this research effort, the illumination set-up underwent a number of design revisions. Initial testing stages involved using a halogen out-door work light. However, to improve flexibility in light orientation and to support modifications in the hyperspectral camera set-up, a 4-prong halogen bulb holder was designed and 3-D printed. A CAD model of the holder is shown in Figure 3.6. All experiments in this thesis utilize only two halogen bulbs, however the holder has the capacity to carry four halogen bulbs.

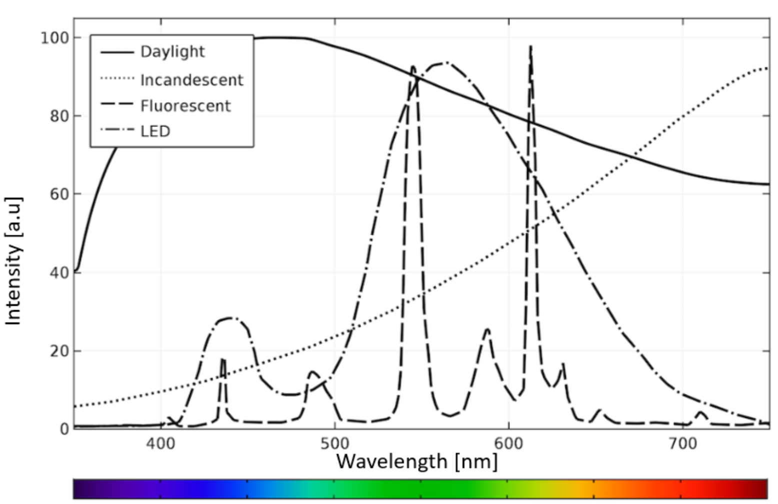

Figure 3.4: Comparison of sunlight, incandescent, fluorescent and LED light emission spectrums. LED and fluorescent lights display discontinuous emission spectrums, while the incandescent is relatively smooth, with its peak energy in the infra-red region. Emission spectrum of halogen lights similar to incadescent lights, but are bluer. Therefore, their peak energy shifts to shorter wavelengths and are comparabled to the spectrum of difused daylight. [5]

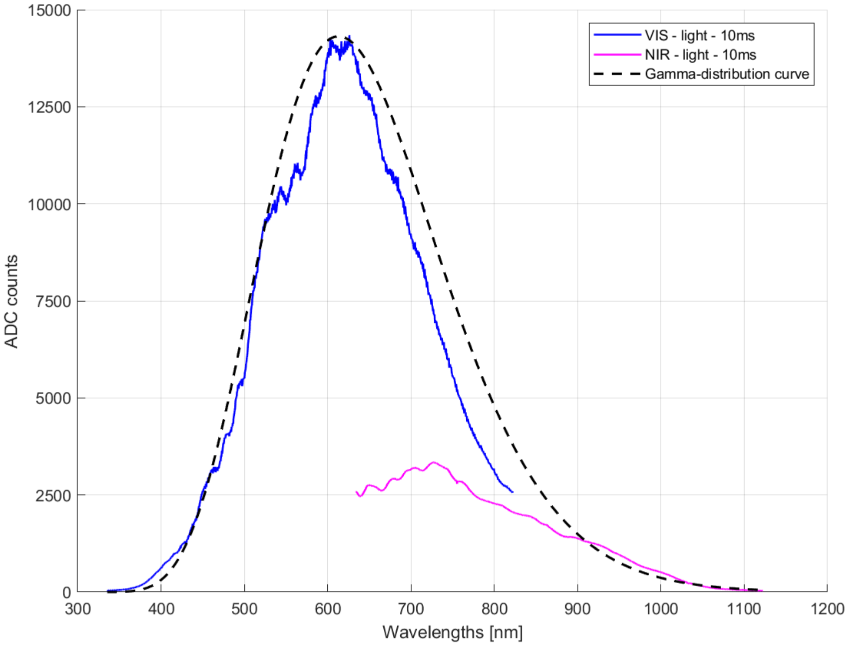

Figure 3.5: VIS and NIR spectrums of Tungsten-Halogen lamps from spectrometer. A general gamma-distribution envelops the spectrum to draw attention to the behaviour of the light in the VNIR region.

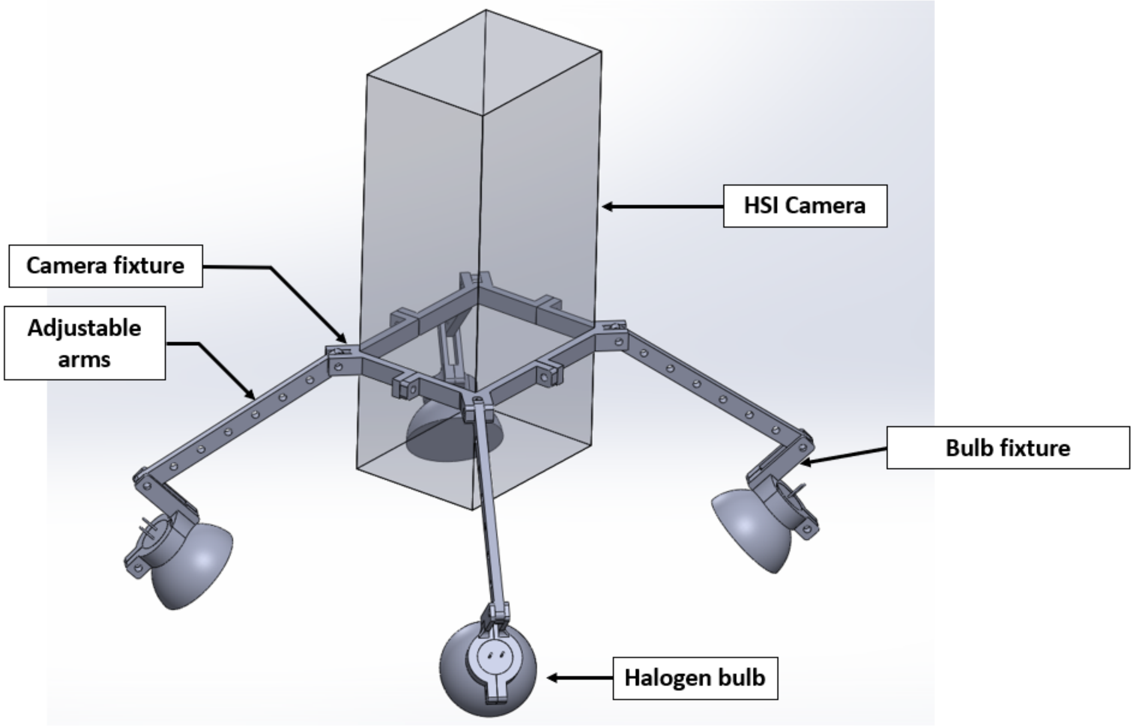

Figure 3.6: CAD model of 4-prong bulb fixture for HSI illumination system. The CAD model shows four bulbs placed in the bulb fixtures, which are connected to the adjustable arms. The arms are connected to the camera fixture at four points. The angle of each arm and each light can be adjusted independently at two points due to the hinge-type design.

3.3 Methodology for Hyperspectral Image Acquisition

The typical steps involved in hyperspectral image acquisition is shown in the flowchart depicted in Figure 3.7. The dark frame is acquired, followed by the white reference and the finally, a hyperspectral image of the region of interest is taken.

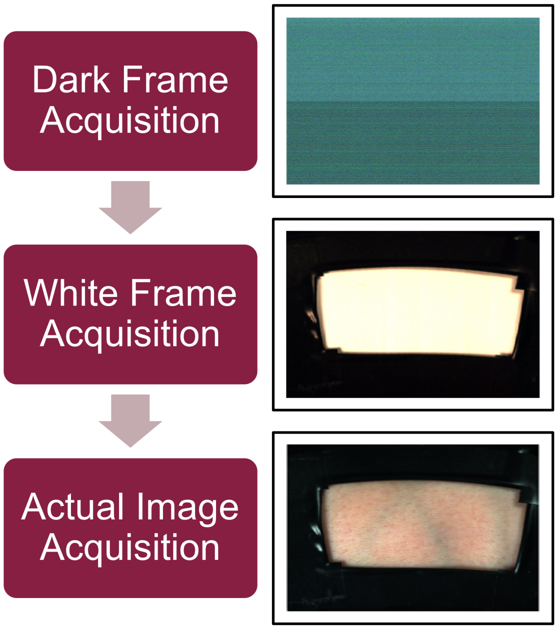

Figure 3.7: A flowchart depicting the experimental paradigm in this thesis, with examples of how the hyperspectral images acquired in each step is visualized in false-color.

The region of interest for all hyperspectral images in the dorsal portion of the hand. This is depicted in panel next to Step 3 in Figure 3.7. An example of what the raw image looks like is depicted in Figure 3.8. A defect that is immediately noticed in the images is the distortion of the rectangle marking the area of interest. This is due to the panning behaviour of the Pan-Tilt Utility, which is rotational about the vertical axis where the system is fixed to the cart. Due to the limited size of the region of interest, the influence of this distortion is not considered during processing. Instead, the edges are cropped out for all images with a fixed aspect ratio.

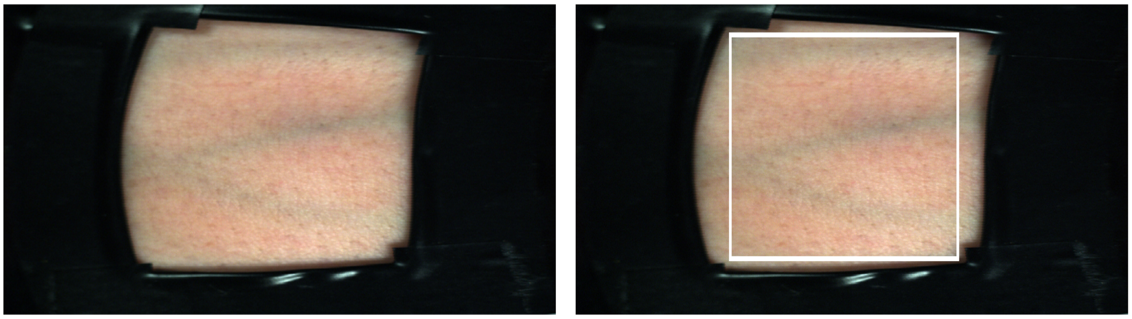

(a) Raw false-color hyperspectral image with distortion

(b) Crop area marked on Hyperspectral image

Figure 3.8: (a) Example of false-color, raw hyperspectral images of the dorsal portion of a subject's hand under the aluminium plate marking the area of interest. Panel (b) shows the part of the image that is cropped for further processing

3.4 Calibration

In any data acquisition system, calibration is a crucial preliminary step. It builds the baseline for any data acquired to be as error-free as possible. In hyperspectral imaging, there are a number of factors that are imperative for accurate and meaningful data acquisition. Having a defined region of interest helps reduce computational burden and enables efficient processing. HSI also requires a reference frame against which the spectral intensities captured are standardized. Like any camera, focused lens and exposure times play a vital role in capturing sharp images and clear spectral data. Furthermore, utilizing the entire dynamic range of the camera is essential to capture the maximum possible information from a scene. These factors collectively contribute to the reliability, accuracy, and interpretability of hyperspectral imaging data. The subsequent sections go through the steps taken calibrate the hyperspectral camera in this study.

3.4.1 Focus and exposure parameters

As mentioned in the previous section, the area of interest was marked using an aluminum cut out beneath which the specimen must be placed. In order to decide a panning distance (X), a datum on the aluminum sheet was marked and used to fix the start and end points of the sweep. This ensured that the specimen or area of interest remained stationary and unchanged between experiments. To focus the lens, 1951 USAF resolution test charts were used in the region of interest. The pan-tilt utility was allowed to run through the controlled sweep distance repetitively while the lens was altered until a desired resolution was obtained. Figure 3.9 shows false-color hyperspectral images before and after focusing. According to the 1951 USAF resolution standard, the resolution to which the camera was focused is 1 line pair per mm, where a line pair refers to a pair of black and white lines [65].

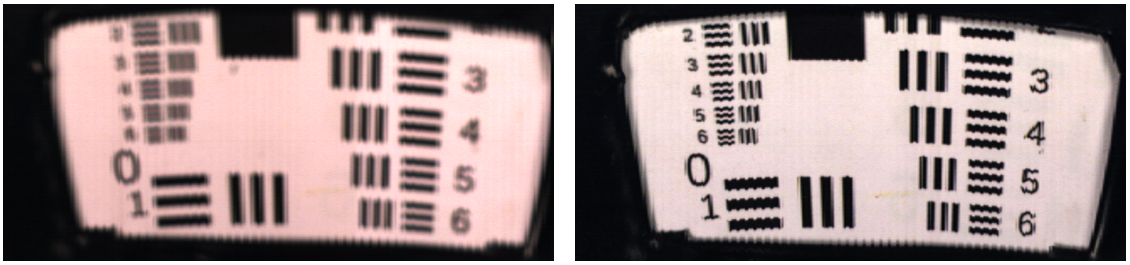

(a) Unfocused hyperspectral images (b) Focused hyperspectral images

Figure 3.9: False-color hyperspectral images before and after focusing to 1 lp/mm resolution according to 1951 USAF standards. The camera lens is adjusted while the PTU is allowed to sweep through a set distance repeatedly. This is done until the desired resolution is achieved.

Additionally, in Figure 3.9, which depicts hyperspectral images of the area of interest, an artifact of the scan is noticed. Due to the panning nature of the Pan-Tilt Utility.

3.4.2 White reference and dark current

In spectroscopy, there is a requirement to obtain interpretable spectral intensities as percent reflectance from raw instrument signal counts. This is accomplished through a white reference frame and a dark frame that accounts for all sensor and illumination artifacts [41]. The white reference helps describe variations in the illumination source and sensor response across a wavelength range by establishing a baseline for the brightest possible response at each spectral band. The dark frame captures the dark current or the minute electric current that persists in photosensitive devices despite the absence of incident photons. The dark frame is just a data cube captured with the lens of the hyperspectral camera closed. The most widely used formulation to convert raw sensor counts in the data-cube of the scene (I) to percent reflectance using a white frame data-cube (WF) and a dark frame data-cube (DF) is as follows:

$$Reflectance\,(x,y,\lambda) = \frac{I\,(x,\ y,\ \lambda) - DF\,(x,\ y,\ \lambda)}{WF\,(x,\ y,\ \lambda) - DF\,(x,\ y,\ \lambda)}, \tag{3.1}$$

Typically, a perfectly reflecting material such as a Spectralon® sheet is used as a white reference to transform the raw instrument data to percentage reflectance of the material. Spectralon® sheets have the highest and most consistent diffuse reflectance of any known material, generally over 99% in a wavelength range of 400 nm to 1500 nm [66]. This makes the sheets extremely expensive, and in response, many research groups have come up with low-cost alternatives. Knighton and Bugbee [6] established that a mixture of barium sulfate and commercial interior white paint can be used as a low-cost substitute. In the same study, white interior paint is noted to have an average percent reflectance of greater than 90% for the wavelength range of 450 nm – 900 nm, which was deemed the most suitable reference for this study. A plot of reflectance measurements with varying percentage of paint and BaSO4 are show in Figure 3.10. An important point to note is that reflectance measurements in the study are done using a reflectance probe that has in-line illumination fiber optics providing a more consistent source of input light.

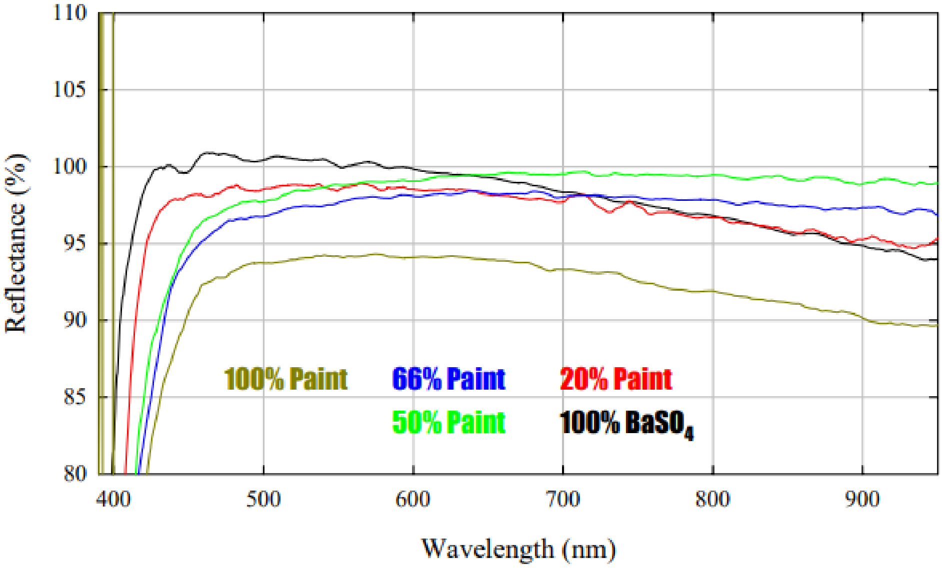

Figure 3.10: Reflectance of pure paint, with successive additions of barium sulphate ($BaSO_4$). Evidently, with the addition of $BaSO_4$, the percentage reflectance measured from the painted samples increases across the wavelength range 450 - 1000 nm. This continues until the mixture contains 50% white paint and 50% $BaSO_4$, before the reflectance falls back down in the wavelength range 600 - 1000 nm [6].

The white reference used in this study is a sheet of cardboard covered in 5 coats of white interior paint. To validate the white reference's usage for the chosen exposure and focus parameters, spectrometer readings as well as hyperspectral images were taken of the white reference and shown in Figure 3.11. Figure 3.11a contains a plot with the spectrometer readings from the halogen light at an integration time of 10 ms and the white reference at an integration time of 50 ms, for comparison. Figure 3.11b shows the spectral data at one pixel on the white reference data-cube. Both plots have data with the dark currents deducted.

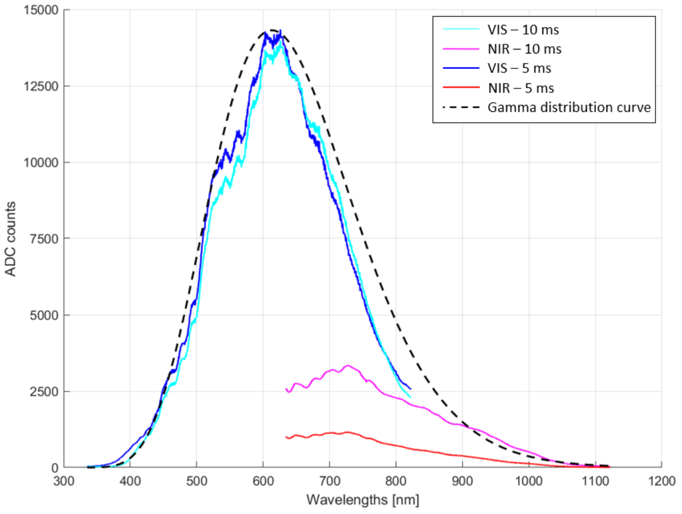

(a) VIS and NIR spectrums for Halogen lamps and white reference from spectrometer

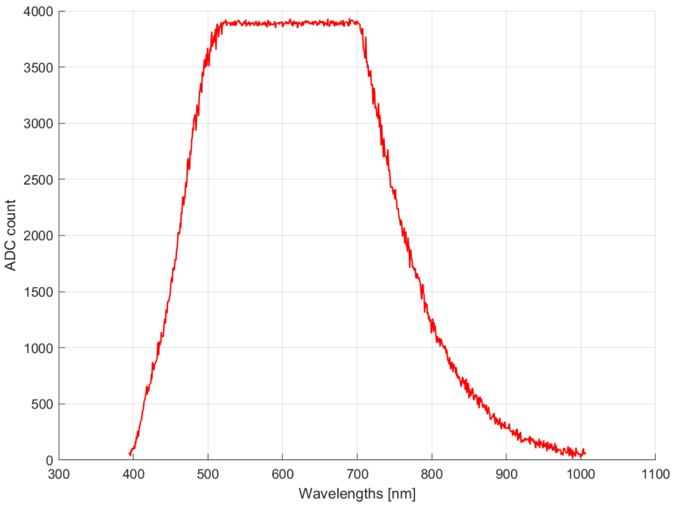

(b) VNIR spectrum of white reference pixel from hyperspectral camera

Figure 3.11: Comparison of measured spectrums from VIS and NIR spectrometers and VNIR hyperspectral camera. The measurement from the HS - camera is clipped between 500 - 700 nm due to saturation of the sensor.

It is evident that the spectral data from the HS-camera follows a trend similar to the halogen light and the white reference captured by the spectrometer. The data follows a right-skewed gaussian curve, which is best explained as a gamma-distribution function. However, at the chosen exposure and focus settings, the white reference signal taken on the hyperspectral camera is clipped due to sensor saturation at 4095 signal counts. It is infeasible to acquire hyperspectral images using a camera with a 12-bit ADC and subsequently convert the raw signal to percent reflectance using white reference data obtained from two spectrometers (VIS and NIR) featuring 14-bit ADCs. Doing so would lead to inconsistencies due to different integration and exposure times and was deemed impractical. Hence, to account for the missing information in the clipped spectrums of the white reference data-cube, the spectrums were modelled with a gamma-distribution curve, as explained in the following section.

3.4.3 Gamma-distribution model for white reference

The gamma distribution is a continuous probability distribution that is commonly used to model positive-value variables with a right-skewed distribution. In general, it is a two-parameter distribution denoted as Gamma(k, θ) where 'k' is the shape parameter and 'θ' is the scale parameter. The probability density function (PDF) of the distribution is as follows:

$$f(x) = \frac{1}{\Gamma(k)\theta^k} x^{k-1} e^{-\frac{x}{\theta}} \tag{3.2}$$

The shape parameter 'k' controls the curvature and skewness of the curve, while the scale parameter 'θ' rescales the distribution. Typical gamma distribution curves are shown in Figure 3.12.

In order to model the white reference using the PDF of the gamma-distribution, a few modifications must be considered. As seen in Figure 3.12, at higher values of 'k', the gamma-distribution becomes more symmetric and morphs into a normal distribution. Therefore, the measured white reference data must be transformed to lie closer to the origin. In addition to this, the function value of the gamma-distribution lies in the interval [0,1], and has to be

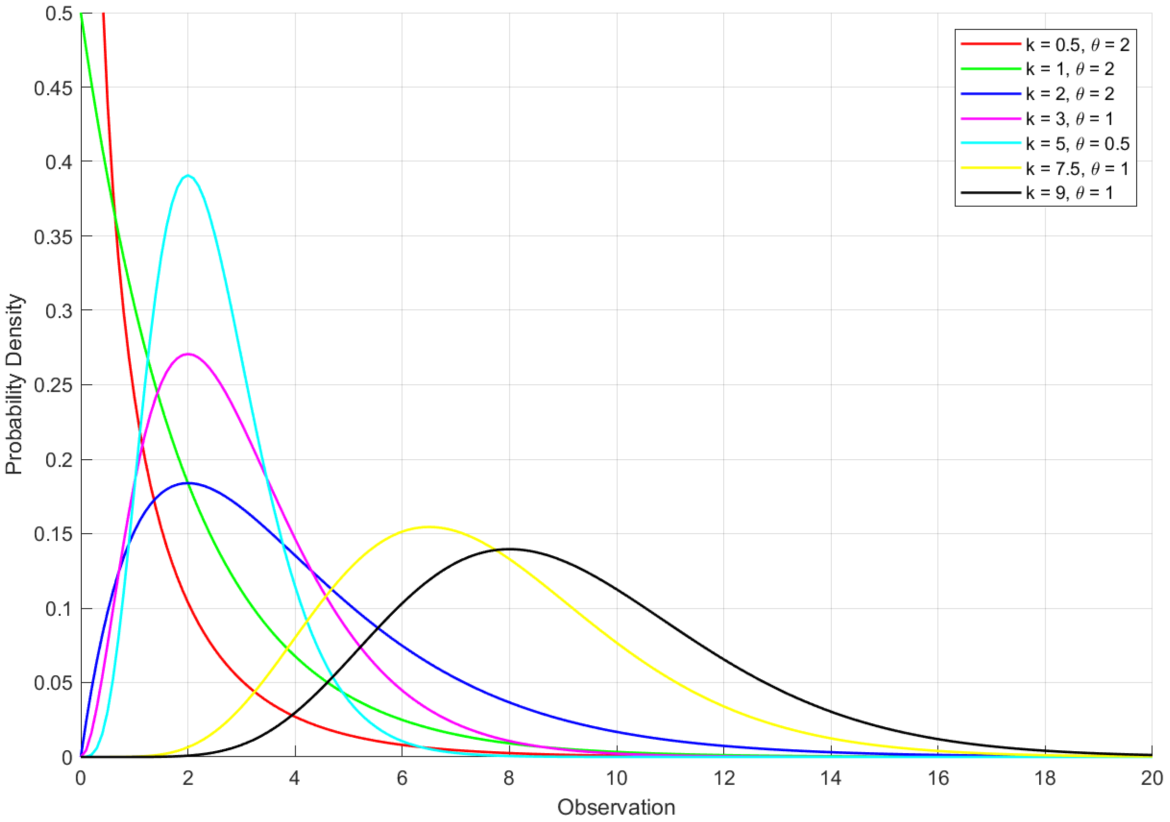

Figure 3.12: Probability density function of Gamma distribution for different shape and scale parameters

rescaled to match the measured white-reference data. To account for these two alterations, an x-transformation term ‘a’ and an additional scaling factor ‘b’ are introduced into the model. The modified gamma-distribution function is as follows:

$$f(x) = \frac{b}{\Gamma(k)\theta^k}(x-a)^{k-1}e^{-\frac{x-a}{\theta}} \tag{3.3}$$

At this point, it is important to highlight the behavior of photosensitive devices, such as CCD cameras, at saturation. When each pixel in the CCD imaging sensor is considered as a container, it can be stated that during saturation, the container becomes completely filled with charge from incident photons. As the container starts to fill, the response of the pixels diverges from linearity [67]. While sensors are designed with this behavior in mind, the divergence from linearity is observed very evidently in Figure 3.13a. In order to avoid its influence in the curve fit, the signal is filtered by 12% from its maximum value before fitting.

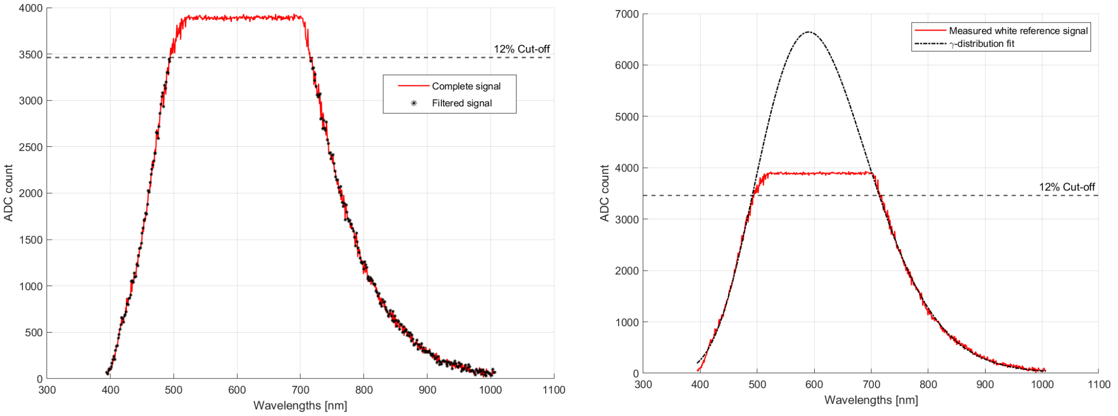

(a) Measured and filtered VNIR spectrum of white reference pixel

(b) Spectrum compensation for white frame with gamma-distribution function

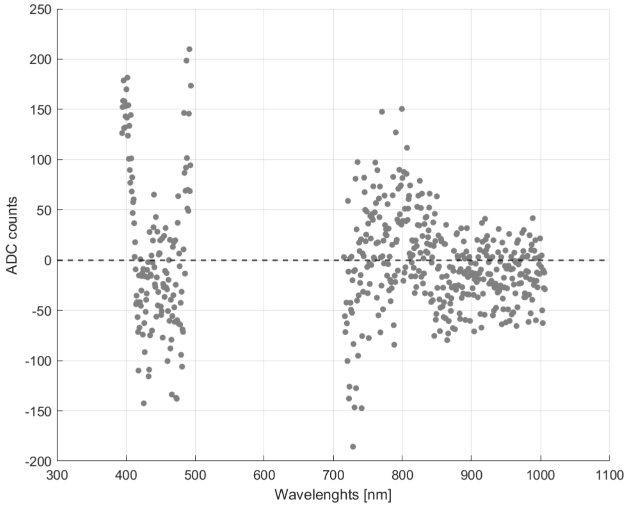

(c) Residual plot for gamma-distribution curve fit

Figure 3.13: Results of gamma-distribution model for white reference

A non-linear least squares algorithm was used to fit the gamma-distribution model to the measured spectrums of the white reference, and the results are shown in Figure 3.13b, with the residuals plotted in Figure 3.13c. The non-linear least squares algorithm results in an accurate representation of the data below the cut-off range, which can be seen in the residuals plot. The maximum error between the model and the data is 209 signal counts, which is about 5.3%. The mean error is 41.419 signal counts, which is well within the acceptable range of 5%. Ultimately, by fitting a curve to the saturated sensor data, the dynamic range of the sensor was increased from 4095 to 6642 signal counts, without discarding the characteristics of the illumination source.

3.5 Summary

This chapter focuses on the image acquisition procedure of hyperspectral imaging set-up used in this thesis. The specifications of the push-broom HSI camera is outlined, followed by a description of the illumination system used to acquire images. The entire hyperspectral imaging cart is displayed a self-sufficient system. The importance of calibration and establishing reference signals in spectroscopy is related with hyperspectral imaging before defining the procedure of calibrating the system used in this thesis. To alleviate the effect of the HSI camera's short-comings, a gamma-distribution function is used to model the entire reference signal that converts imaging sensor counts to interpretable reflectance percentages.

Chapter 4

Theory

An intrinsic property of organic and inorganic materials is their ability to interact with electromagnetic radiation. There are mainly five processes that define light-matter interactions in materials: reflection, refraction, absorption, scattering and transmission. Throughout these interactions, the fundamental law of energy conservation is maintained, ensuring that energy is neither created nor destroyed, but rather transformed [51]. The manipulation of light by these materials through absorption, reflection and scattering is what gives them a particular color appearance. To derive meaningful skin characteristics from hyperspectral data, it is essential to apply a mathematical model that embodies these behaviors of the skin. This model will enable the transformation of raw hyperspectral data into valuable insights about the skin's properties. This chapter covers some basics of light-matter interactions in biological tissues, followed by a detailed breakdown of the mathematical model used to represent human skin in this thesis and the parameters and assumption involved in building the model.

4.1 Scattering and absorption in biological materials

In the case of turbid materials like biological tissues, understanding absorption, scattering and transmission processes is crucial, as these processes dominate the tissue's optical characteristics. The energy E of an incident photon of light is inversely related to the light's wavelength and is given by E = hf = hc/λ, where c is the speed of light in vacuum, and h is Planck's constant. During absorption, a portion of the energy carried by the photon is attenuated by molecules in the material. The electrons in these molecules capture the energy and undergo transition to an excited or high-energy state. This phenomenon is highly selective, where the molecules only absorb light of specified wavelengths. The electron eventually drops back down to a neutral or grounded state by emitting the energy as electromagnetic radiation at a different wavelength (fluorescence) or through heat dissipation, or vibrational transitions [68]. The constituent part of a material that is responsible for its color by absorbing different regions of the electromagnetic spectrum are known as chromophores. The absorption coefficient of a material is the parameter used to describe the effectiveness of chromophore to absorb light. This property has units of 1/length [cm^{-1}], where the length is related to distance travelled by the incident photon of light before being absorbed. Absorption results in a unique spectral signature for each material, which contains the remaining unabsorbed energy [51]. For inhomogeneous materials like biological tissues, these spectral signatures can be used to distinguish between its different components.

However, it is important to realize that the remaining part of the electromagnetic spectrum that does not get absorbed undergoes a blend of the four other light-matter interaction processes in inhomogeneous materials. Depending on the refractive index and surface contours of the material, a small part of the incident light is directly reflected back. A large part of the incident light is scattered. Scattering refers to the phenomenon where light deviates from its original path due to interactions with the material's constituents, and hence is no longer part of the incident beam, but still present as diffused light. This could be in any direction, through the material or in the opposite direction (termed back-scattering). As the photons travel through the material (transmitted), they undergo successive scattering and absorption, contingent on the concentration of absorbing constituents present. Similarly, scattering coefficient is described by the same unit of 1/length [cm^{-1}], and indicates how quickly the incident photons would lose energy to redirection. There are mainly two types of scattering mechanisms: Mie and Rayleigh scattering. Understanding these fundamental scattering mechanisms is integral in modelling the interaction between inhomogeneous media and light [68].

Mie scattering deals with scattering of light by particles that have comparable size to the wavelength of light. The Mie theory particularly explains the scattering of electromagnetic planes by a homogenous sphere [69]. A practical example would be the white appearance of clouds; light from the sun is diffused or scattered by droplets in the cloud to appear white [70]. Mie theory is not heavily reliant on wavelength, however mathematical approximations of the theory call for an involvement of wavelength of incident light. In fact, Rayleigh scattering approximates the Mie theory for when the size of the particle is significantly smaller than the wavelength of light. The amount of Rayleigh scattering is inversely proportional to the fourth power of the wavelength of incident radiation. This phenomenon is observed in everyday life when the earth's atmosphere scatters the shorter wavelengths of the sun's electromagnetic radiation, causing the sky to look blue during daytime. Similarly, the reddening of the sky around the sun during sunset is also due to Rayleigh scattering, when the sunlight is forced to travel a longer distance through the earth's atmosphere, scattering the higher wavelengths [71].

The human skin is modelled using a blend of the aforementioned contributing factors of attenuation. Photons that enter the skin must undergo a series of scattering and absorption events before coming of the skin. The photons that return from the skin through back-scattering impart the skin its color. In this thesis, the back-scattered energy from human skin is modelled by numerical simulation involving a fusion of Kubelka-Munk [56] and Beer-Lamber-Bouguer laws [72], with special importance given to the influence of wavelength in the depth of penetration of light. A number of authors such as Alcaraz de la Osa et al. [73] and [74] have applied the aforemention theories to model diffuse reflectance spectra. Moreover, Wan et al. [75] proved the capability of using the Kubelka-Munk theory to model the optical of in-vivo and in-vitro skin. With these foundational studies in mind, the following sections delve into the framework of the numerical study conducted in this thesis.

4.2 Mathematical model of the human skin

The human skin is composed of three fundamental layers, the epidermis, the dermis and the hypodermis or the subcutaneous layer. Each layer can be further divided into sub-layers and contain a variety of cells that are responsible for pigmentation, hair growth, sweat production and UV protection. In this study, for the sake of simplicity, the skin is limited to two layers – the epidermis and dermis. The bilayer structure of the human skin model is shown in Figure 4.1.

The epidermis is approximately 100 µm thick and contains melanocytes, keratinocytes, and Langerhans cells. These cells in the epidermis contain mainly one chromophore - the melanin produced by melanosomes, which absorb and are stimulated by ultra-violet radiation (290-400 nm). The concentration of melanin is the only factor in the epidermis that determines the range of color seen in normal human skin, which can vary from slightly yellowish to dark brown. It was noted that the scattering in the epidermis is minimal as a consequence of irregular refractive index than any particulate scattering agents [51].

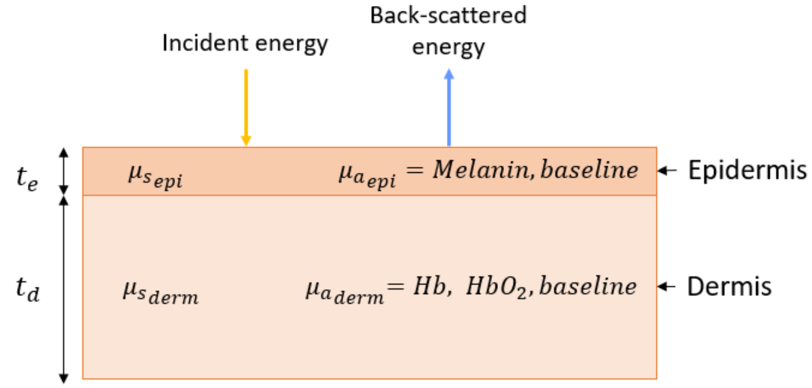

Figure 4.1: Bi-layer model of the skin with coefficients of absorption and scattering for the two layers: the epidermis, and the dermis. The incident energy (yellow) undergoes numerous absorption and scattering events before coming out as back-scattered energy. This back-scattered energy is picked up by a measurement device, such as a hyperspectral camera.

On the other hand, the dermis is an optically thick medium containing both scattering agents and chromophores. The primary scatters of visible light in the dermis are collagen fibers, that have significantly different refraction of index than their surroundings. Even though the size of these scattering centers is much smaller than the visible, it was determined that the wavelength dependence of the scattering is only $\lambda^{-1.5}$. Chromophores in the dermis include the oxy and deoxy hemoglobin, each of which have distinct absorption spectrums. The absorption of visible light by hemoglobin in the capillaries and arteries gives a reddish hue to human skin. Veins appear dark blue due to Rayleigh scattering that backscatter blue more strongly than red [51].

Besides these chromophores and scattering agents, human skin contains fat, water, -carotene, and bilirubin as well. These constituents each have their own absorption spectrum and wavelength dependent scattering behavior. However, in this study, the main chromophores are considered to be only melanin, oxyhemoglobin and deoxyhemoglobin, whose absorption spectrum are taken from the database created by Prahl [76]. Wavelength dependent scattering coefficients for the epidermis and the bloodless dermis are also obtained from the same database. These spectrums are shown in Figure 4.2 .

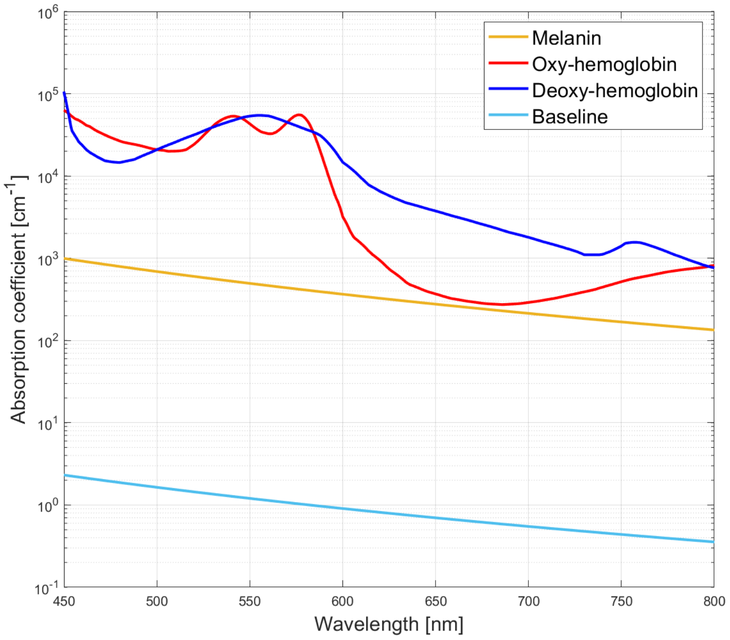

Figure 4.2: Absorption coefficients of skin chromophores: melanin, oxy-hemoglobin, deoxy-hemoglobin, and the baseline absorption due to fat and water. Two distinct peaks are observed between 500 - 600 nm in the absorption spectrum of oxy-hemoglobin (red), which is later observed in the model as well as measured data.

4.2.1 Beer-Lambert-Bouguer Law

Also known simply as the Beer-Lambert Law [72], it is a fundamental law in spectroscopy that describes a relationship between the optical attenuation of a physical material containing N attenuating species of uniform concentration, to the optical path length through the sample and the absorptivity of the species [5]. This relationship is described in Equation (4.1).

$$A = \sum_{i=1}^{N} \varepsilon_i \int_0^l c_i(x)dx \tag{4.1}$$

where A is the absorbance or optical attenuation in the material, ε_i is the molar extinction coefficient of the attenuating species, c_i is the concentration of the attenuating species and l is the path length of the beam of light through the material. For a uniform path length l, this expression can be rewritten as Equation (4.2).

$$A = l \sum_{i=1}^{N} \varepsilon_i c_i \tag{4.2}$$

In spectroscopy specifically, the wavelength dependent attenuation or absorption coefficient of a mixture in solution containing N species at different concentrations is given in Equation (4.3). The total absorption coefficient of a material has a unit of $cm^{-}1$, and can be substituted in Equation (4.2) to get the total attenuation in that particular material.

$$\mu = log10 \sum_{i=1}^{N} \varepsilon_i c_i \tag{4.3}$$

Equation (4.3) can be we applied to the individual layers of the skin to obtain the total absorption coefficients of the epidermis (K_{epi}) and the dermis (K_{derm}). This is given in Equation (4.4) and Equation (4.5), respectively.

$$\mu_{epi} = (f_{mel}\mu_{mel} + (1 - f_{mel})\mu_{baseline})log(10) \tag{4.4}$$

$$\mu_{derm} = ((f_{blood}SpO2\mu_{HbO_2}) + (f_{blood}(1 - SpO2)\mu_{Hb}) + (1 - f_{blood})\mu_{baseline})log(10) \tag{4.5}$$

In Equation (4.4) and Equation (4.5), the subscripts 'mel', 'HbO_2' and 'Hb' refer to melanin, oxy-hemoglobin and deoxy-hemoglobin respectively. The concentration of oxy-hemoglobin and deoxy-hemoglobin are modelled using the oxygen saturation in the blood (SO) and the blood volume fraction in the dermis (f_{blood}). Here, a blanket baseline absorption coefficient is considered to model fat, water, and the attenuation due to the remaining skin cells present in both the dermal and epidermal layers. These absorption coefficients are then used to develop the total reflectance at the surface of the skin in the following section.

4.2.2 Kubelka-Munk Theory

The Kubelka-Munk Theory [56] is a widely used model for describing light interaction with multilayered media, such as paint layers. It assumes that the medium consists of a large number of infinitesimally thin layers, and each layer has uniform optical properties. This theory provides a mathematical framework to predict the reflectance and transmittance of a medium as a function of its thickness, the refractive index, and the absorption and scattering coefficient of each layer.

To develop the mathematical model, the fundamental differential equations of the Kubelka-Munk theory must be derived. Consider a planar parallel coating of a thickness X with absorption coefficient a and scattering coefficient s on a substrate, as shown in figure. Incident light with intensity I is shone on the coating, of which a portion J is reflected back. The reflected intensity J can be written as $J = RI$, where R is the reflectance or albedo of the coating. The albedo, or reflectance of a material can be considered analogous to a transfer function of a system and describes the relationship between the input and output of a system.

Consider, at an arbitrary distance x from the lower surface of the coating, layer P of infinitesimal thickness dx. This layer P has light intensity i going downwards, and back-scattered light intensity j going upwards, both results of reflection, refraction, transmission, and scattering. Assume that the infinitesimal layer P absorbs a portion adx and scatters a portion sdx of the light passing through the layer. The change in the intensities of the light passing through the layer due to absorption and scattering can be written as the two fundamental differential equations given in Equation (4.6), and Equation (4.7). The first term in both equations refer to the portion of the light lost to absorption and scattering while passing through the layer. The intensity of light lost due to scattering of downward travelling light $(sjdx)$ is then added to the change in intensity of the upward travelling light (di), and vice versa. This addition is given by the second term in both equations.

$$-di = -(\mu_a + \mu_s)idx + \mu_s jdx \tag{4.6}$$

$$dj = -(\mu_a + \mu_s)jdx + \mu_s idx \tag{4.7}$$

Since both of these equations must be solved simulatenously to obtain the total reflectance of the layer, the equations can be added and simplified using the substitution $r = j/i$ which is the reflectance in the infinitesimally thin layer, analogous to the previous definition of reflectance of the coating (R = J/I). The combined differential equation that can be used to obtain the reflectance of each layer is:

$$\frac{dr}{dx} = \mu_s(r^2 - 2\frac{\mu_a + \mu_s}{\mu_s}r + 1) \tag{4.8}$$

Equation (4.8) can be integrated over the entire thickness of the coating to get the reflectance on the surface of the coating, starting with the reflectance of the substrate. In the next section, an adaption of this theory is numerically solved to simulate the reflectance of the different layers of the skin.

4.2.3 Numerical Simulation of skin reflectance

In the present study, the human skin is modelled as a bilayer structure, as shown in figure, with the epidermis laying on top of the dermis. The theoretical model developed in the Kubelka-Munk theory is adapted to layers of the skin, and numerically solved through the thickness of the skin. To do so, a few assumptions about human skin must be made. The distribution of chromophores and scattering agents are assumed to be homogeneous and isotropic within each layer. This implies that the chromophores' absorption coefficients, and the scattering behaviors are uniform in all directions. Both the dermis and epidermis are assumed to be finitely thick in this model. According to Sandby-Møller et al. [77], mean epidermal thickness in the dorsal forearm is estimated to be around 56.6 µm. Similarly, Van Mulder et al. [78] estimated the mean thickness of all the layers of the skin in the same region to be 1.44 mm.

According to the Kubelka-Munk theory, the reflectance on the surface of a planar coating depends on the absorption and scattering coefficients of the coating. In the case of human skin, the epidermal and dermal absorption coefficients are derived in Section 4.2.1 as μ_{epi} and μ_{derm} using the Beer-Lamber-Bouguer law. Additionally, scattering in the two layers must also be defined, as the reflectance from the turbid, bloodless layers of the skin is dominated by scattering. Literary references point to a variety of scattering coefficients for the skin, and assume the same scattering coefficient for the epidermal and dermal layers in the skin. Typically, it is a combination of Mie and Rayleigh scattering. Rayleigh scattering is highly wavelength dependent and has an inverse relationship with λ^4. Mie scattering is particle size dependent and very weakly dependent on wavelength. However, to model this scattering, the coefficient is defined as a multiple of λ^b, where b varies from 0 to -2. This variation could be attributed to differences in specimens, illumination systems and measurement data. Keeping this in mind, the total scattering of the epidermal and dermal layers is defined using two parameters A and B, as shown in Equation (4.9).

$$\mu_s = a\lambda^b + 1.1 \times 10^{12}\lambda^{-4} \tag{4.9}$$

Hence, the reflectance formulation derived in Section 4.2.2 as Equation (4.8) can be rewritten using the epidermal and dermal absorption coefficients as Equation (4.10) for epidermal layers and Equation (4.11) for the dermal layers. In the numerical simulation, the two following equations are integrated over the thicknesses of the epidermis and dermis, for every wavelength λ in a given range.

$$\frac{dr}{dx}(\lambda) = \mu_s(\lambda)(r^2 - 2\frac{\mu_{epi}(\lambda) + \mu_s(\lambda)}{\mu_s(\lambda)}r + 1) \tag{4.10}$$

$$\frac{dr}{dx}(\lambda) = \mu_s(\lambda)(r^2 - 2\frac{\mu_{derm}(\lambda) + \mu_s(\lambda)}{\mu_s(\lambda)}r + 1) \tag{4.11}$$

4.2.4 Wavelength dependent thickness function

As explained earlier, when photons travel in a material, the amount of absorption and scattering is dependent on the distance travelled by the photon. Furthermore, penetration depth is a measure of how far electromagnetic radiation can travel through a material before its energy is attenuated to 37% of its original value. In the case of biological tissue, there exists a wavelength range where electromagnetic radiation has maximum depth of penetration. This window is between 650 nm to 1350 nm and is termed as the therapeutic window or optical window of biological tissues [79]. A parallel can be drawn to the optical window of the earth's atmosphere, which is between 300 nm to around 2000 nm. This is a driving factor in the earth being inhabitable by living organisms since plants use UV radiation (300 nm) to produce energy and the higher wavelengths (greater than 1000 nm) dictate suitable temperatures on the earth's surface. Figure 4.3 shows the schematic of the depth to which different regions of the electromagnetic spectrum penetrates the skin.

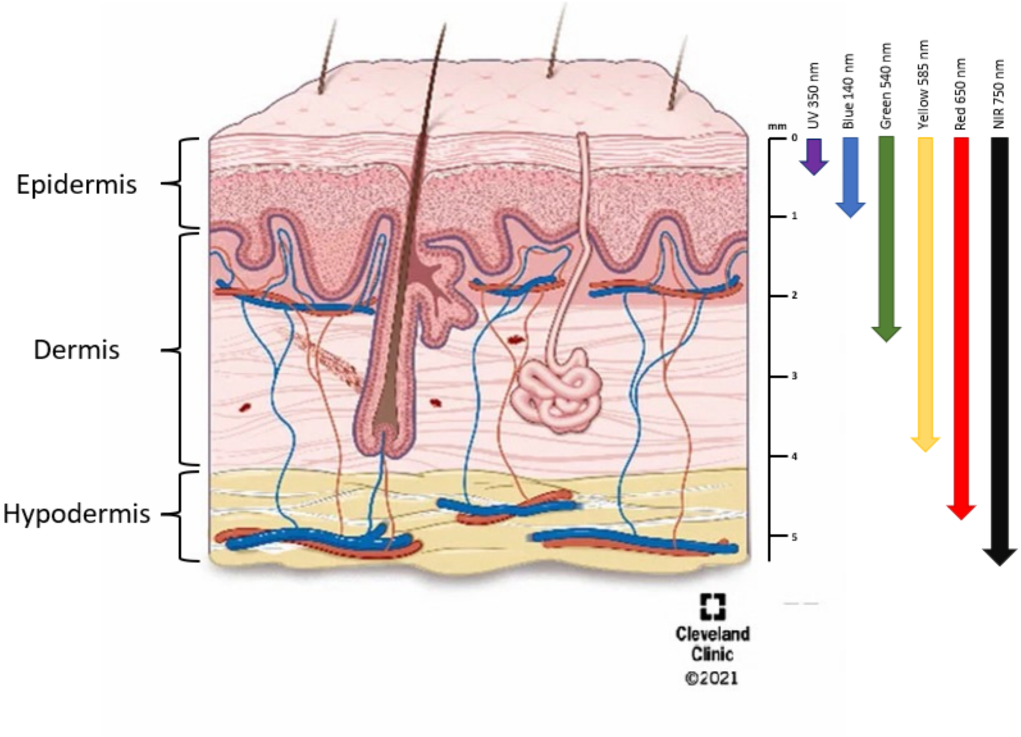

Figure 4.3: Penetration of light into the skin across the electromagnetic spectrum, adapted from Cleveland Clinic's diagram of the Layers of the Skin [7] and Clement et al. [8]. The skin is shown to have three distinct layers in this image: the epidermis, dermis and the hypodermis or subcutaneous layer. As one moves down the electromagnetic spectrum from shorter to longer wavelengths, light penetrates deeper into the skin, due to more resistance to scattering.

To incorporate this optical window in the numerical model, a wavelength dependent function was used to determine the depth of penetration at a particular wavelength. The function was in accordance with the findings of Bashkatov et al. [9]'s estimation of the depth of penetration, as shown in Figure 4.4.

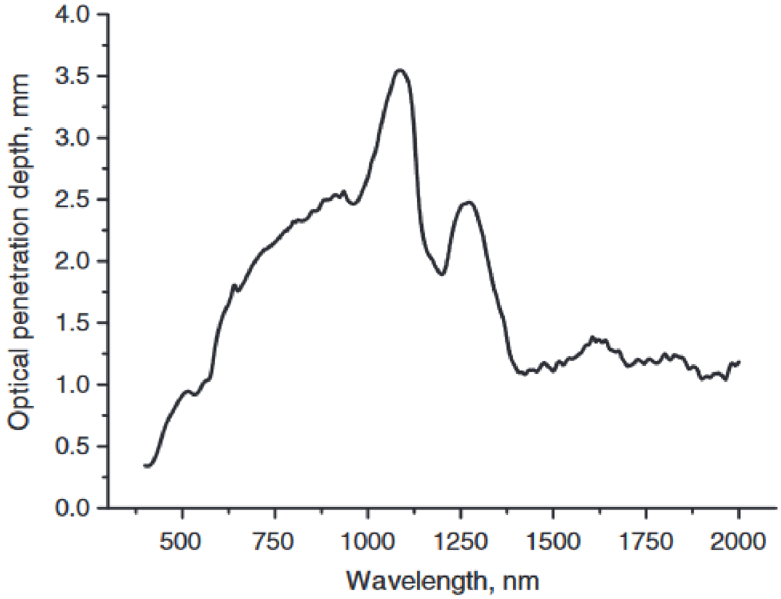

Figure 4.4: Estimated depth of penetration of light into the skin, replicated from [9]. A function that mirrors this graph in the 400 - 1000 nm range is used to model the depth of penetration of light with respect to wavelength.

4.3 Objective function

The intention of building a mathematical model for a physical phenomenon is to control and isolate variables that contribute to the phenomenon. In our case, the goal is to extract usable information from hyperspectral images of the skin, with the support of biological properties. The parameters that can be extracted from the mathematical model of the skin are volume fractions of melanin, blood and the oxygen saturation of the blood. Additionally, since the amount of scattering in the skin is so highly variable, it can also be extracted. Studies have shown that these parameters are influential biomarkers in the skin, and can help distinguish between different specimens and samples. To make sure the parameters extracted can help future decision making, the model developed in Section 4.2 must be evaluated and validated.

Mathematical optimization is a common approach to validate and extract parameters from mathematical models. The process involves the selection of best fitting variables in a model, given an objective function. Typically, to extract parameters from a model so that it best fits a measured response, the objective function is defined as the minimum of the Euclidean distance between the two. This can be interpreted as minimizing the L_2 norm of the difference between the measured and mathematical responses. The objective function, in addition to its constraints that is minimized in this study is given in (4.12).

In Equation (4.12), x refers to the vector of design variables $[f_{mel}, f_{blood}, SO, A, B]$, whose definitions are same as in the mathematical model. The listed inequality constraints in Equation (4.13) are upper and lower bounds for the design variables, where c_1 refers the upper bound of melanin content depending on the individual that is imaged. R_{meas} refers to the measured and white-reference calibrated spectrum of a pixel in the hyperspectral image. R_{theor} is the theoretical value of reflectance obtained from the mathematical model, which depends on the design variables in x, and also exists as a spectrum with a specified wavelength range.

$$min\ f(x) = \sum_{\lambda=1}^{N} (R_{meas}(\lambda) - R_{theor}(x, \lambda))^2 \tag{4.12}$$

Subject to

$$
\begin{aligned}
g_1(x) &: 0.001 - x(1) <= 0 \\
g_2(x) &: x(1) - c_1 <= 0 \\
g_3(x) &: 0.001 - x(2) <= 0 \\
g_4(x) &: x(2) - 0.1 <= 0 \\
g_5(x) &: 0.75 - x(3) <= 0 \\
g_6(x) &: x(3) - 1 <= 0 \\
g_7(x) &: 1 \times 10^3 - x(4) <= 0 \\
g_8(x) &: x(4) - 1 \times 10^{10} <= 0 \\
g_9(x) &: -2 - x(5) <= 0 \\
g_{10}(x) &: x(5) <= 0
\end{aligned}
\tag{4.13}
$$

4.4 Summary

This chapter outlines the theory involved in light-matter interactions, specifically concerning biological tissues. Scattering and absorption processes in these tissues are explained, with mathematical formulation using the Beer and Lambert laws and the Mie theory for scattering. The Kubelka-Munk theory is introduced as a means to apply these theoretical concepts to the model the human skin, containing numerous absorption and scattering agents. These absorption agents are termed chromophores and are identified to be melanin and blood (oxygenated and de-oxygenated) in the skin. The model is then derived using all the theoretical concepts, including the influence of wavelength on the depth of penetration of light in the skin. Ultimately, the aim of this chapter centers on formulating an objective function that effectively leverages measured diffuse reflectance data to obtain valuable insights.

Chapter 5

Results and Discussion

In this thesis, the main goal is to extract meaningful insights from the measured hyperspectral data of human skin. So far, the working of a hyperspectral camera in the context of capturing information from a scene is thoroughly examined. Next, the theory behind absorption and scattering phenomena occurring in the world was outlined, with a specific focus on its application to biological tissues. These phenomena were recognized to be wavelength dependent, and the importance of understanding the influence of wavelength was highlighted. Therefore, a mathematical model was described to embody these interactions between biological tissues and incident light was shown. In this chapter, the outcomes of acquiring hyperspectral images from different subjects and applying the model to these measurements are depicted. The model's sensitivity to the different variables is also explored, to determine which wavelengths can be leveraged to extract the most information.

5.1 Hyperspectral Images of skin

The process of capturing hyperspectral images of human skin involves three steps: darkframe acquisition, white reference acquisition and skin section image acquisition. In a typical acquisition sequence, these three steps are carried out in the order listed. Capturing the darkframe requires one sweep of the camera with the lens closed. Then, the white frame is acquired, using the white reference sheet described in Chapter 3. Finally, hyperspectral images of human skin are captured by placing the dorsal part of a patient's hand under the aluminum fixture marking the region of interest. The exposure time is kept constant for all three acquisitions at 5000 μs. This setting is maintained across all patients and images acquired.

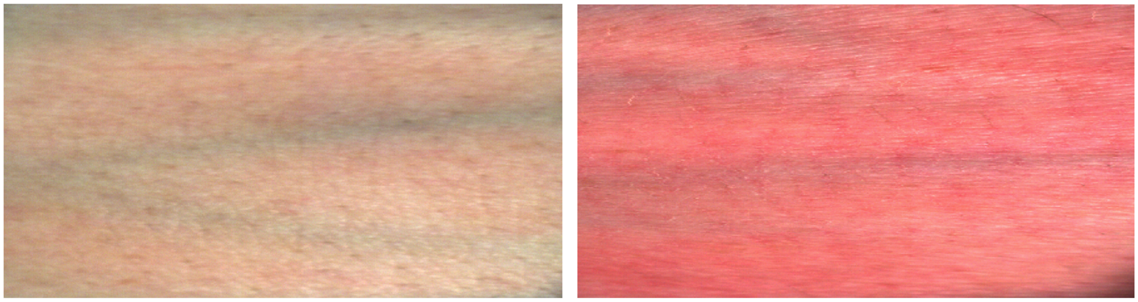

(a) Subject A (b) Subject B

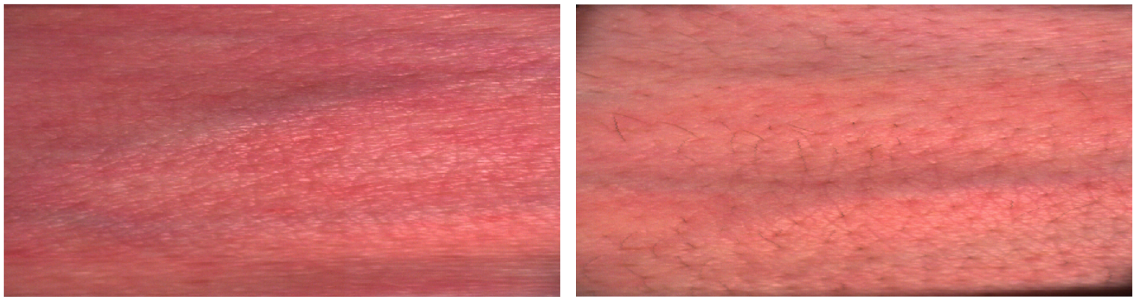

(c) Subject C (d) Subject D

Figure 5.1: Hyperspectral images of dorsal side of the hand of all subjects in Set-1. All images are displayed in false-color with three selected wavelengths in the RGB regions of the electromagnetic spectrum. The bands selected are 650 nm for red, 550 nm for green and 470 nm for blue.

Initial studies focused only on Caucasian male volunteers in their early twenties. Data obtained from these volunteers will be categorized under 'Set-1' and the volunteers are referenced as 'Subject A', Subject B', 'Subject C', 'Subject D' to maintain anonymity. The hyperspectral images displayed are raw signal counts with the dark current subtracted. The images shown in Figure 5.1 are false-color RGB representations of the hyperspectral images obtained from Set-1. The bands chosen in RGB are 650 nm for red, 550 nm for green and 470 nm for blue for all images.

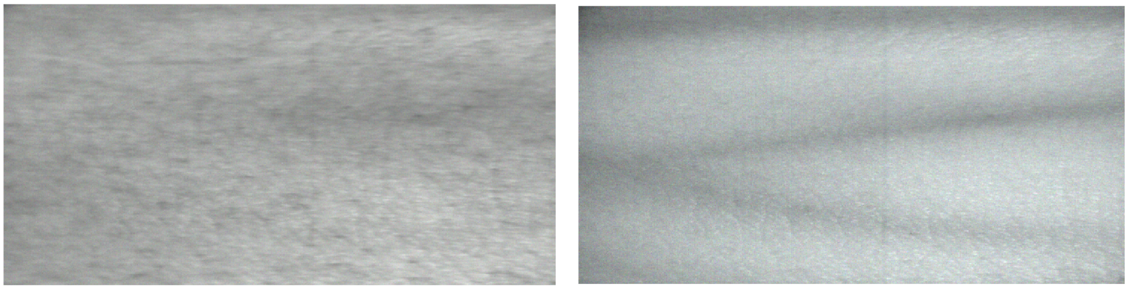

(a) Subject A - 540 nm

(b) Subject A - 800 nm

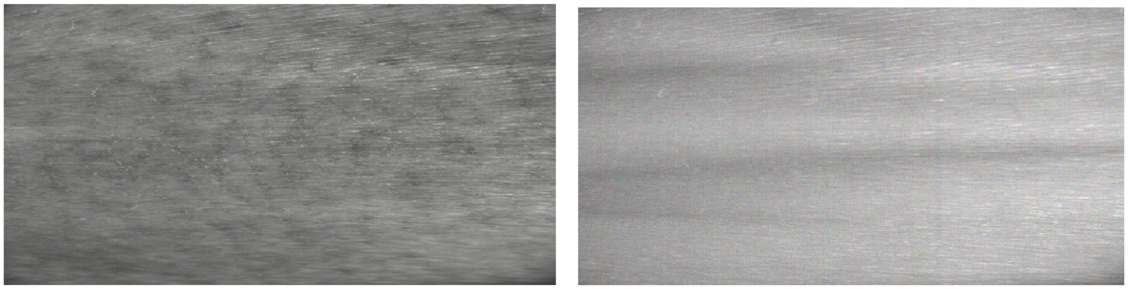

(c) Subject B - 540 nm

(d) Subject B - 800 nm

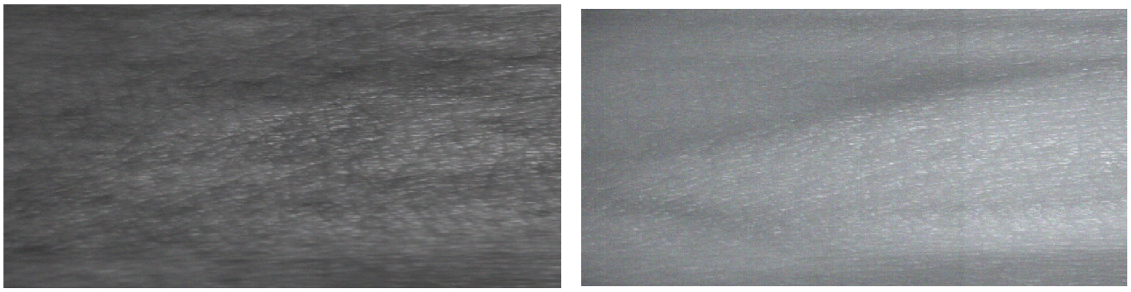

(e) Subject C - 540 nm

(f) Subject C - 800 nm

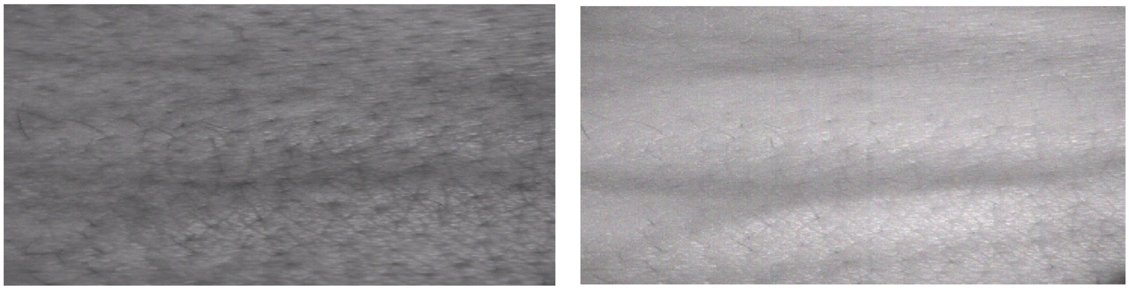

(g) Subject D - 540 nm

(h) Subject D - 800 nm

Figure 5.2: Comparison of Hyperspectral images in Set-1 at shorter and longer wavelengths. Intensity values at 540 nm (green) in the hyperspectral data-cube are used to display the images of Set-1 at the shorter wavelengths. Similarly, intensity values at 800 nm (near-infrared) is used to display the images of Set-1 at longer wavelengths.

MATLAB's Hyperspectral Imaging Toolbox [80] is used to visualize all hyperspectral images. An initial observation in hyperspectral images of the skin is the drastic change in the image frames at the shorter and longer wavelengths. Since each frame or band of the data-cube represents the intensity of back-scattered light at a specific wavelength is a page in the book, we can select and visualize bands of interest as 2-D images. The distinction observed between shorter and longer wavelength bands is reasonable, due to the fact that light at shorter wavelengths having more energy travels shorter distances within the skin, while the longer wavelength light penetrates deeper and interact with the blood in the embedded veins. This is clearly visible in Figure (5.2) for Set-1. Mottled regions are observed in Figure (5.2a), Figure (5.2c), Figure (5.2e), Figure (5.2g), denoted presence of melanin on the superficial epidermis. Similarly, the presence of veins in the dermis is depicted in Figure (5.2b), Figure (5.2d), Figure (5.2f), Figure (5.2h) as a network of dark strands traversing the image horizontally.

The second collection of images consisted of two Caucasian male volunteers in their early twenties and two brown male volunteers, one in the young adult age group and the other in his early twenties. This collection of images will be termed 'Set-2', with volunteers referenced as 'Subject A', Subject B', Subject E'(young adult), 'Subject F', as the first two subjects are repeated from Set-1. Additionally, subjects in Set-2 were requested to get the blood flowing in their arms by lifting something heavy a few minutes before imaging. Figure 5.3 depicts the raw hyperspectral images, where for Caucasian subjects A and B, the skin appears extremely red for regions where there is no vein present. Furthermore, a common observation in all the images is the clear presence of veins as blue-greenish or darker regions. It must be noted that the veins and skin regions themselves may not have this color, they appear so due to the bands that are selected to depict the false-color images.

A point to note is that it is not logical to process the entire image for model validation

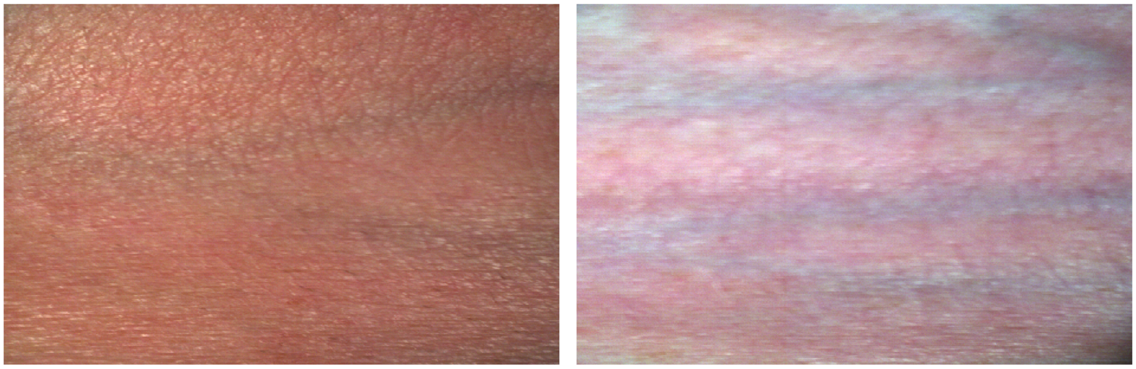

(a) Subject A (b) Subject B

(c) Subject E (d) Subject F

Figure 5.3: Hyperspectral images of dorsal side of the hand of all subjects in Set-2. All images are displayed in false-color with three selected wavelengths in the RGB regions of the electromagnetic spectrum. The bands selected are 650 nm for red, 550 nm for green and 470 nm for blue. Subject E (c) and Subject F (b) are subjects with higher melanin content.

and visualization; instead, we can choose pixels with expected outcomes and predefined nominal ranges for skin chromophores. This is also convenient, as the computational time for converting the entire image to percentage reflectance using the calibration methodology outlined in Chapter 3 is enormous due to the sheer size of the image. Therefore, pixels of interest are selected and converted to percentage reflectance with reference to the white reference spectrum. Figure 5.4 shows two selected pixels in Subject A's raw hyperspectral image, one in a region where a vein is clearly present, and one where there is no obvious vein, which is termed 'skin'.

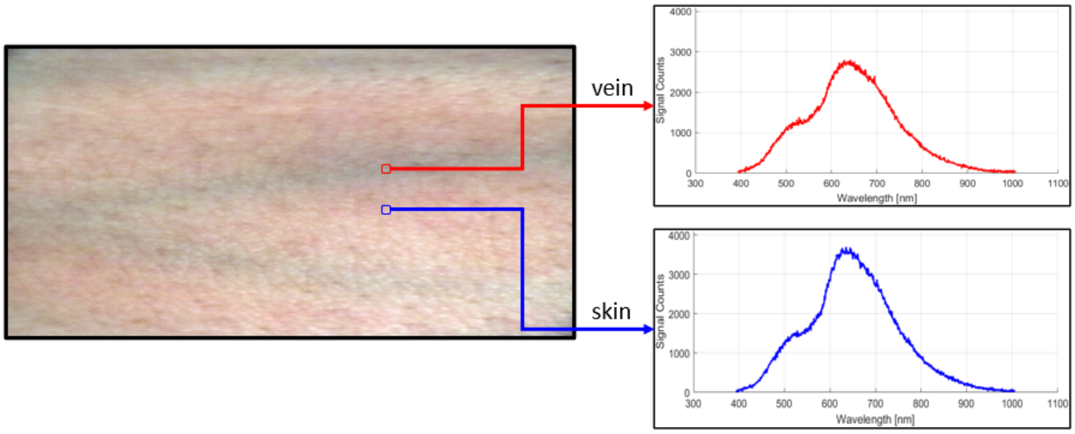

Figure 5.4: Raw spectrums from selected pixels. Pixels are selected from venous and non-venous (skin) regions that are visually evident in the false-color images of the skin. The raw spectrums of a pixel in the venous region and skin regions are displayed in red and blue respectively. The spectrum of skin has higher magnitude when compared with the vein, indicating higher absorption at these venous regions.

Moving forward, the pixels will be represented as spectrums of percent reflectance and not as pure signal counts. Pixels of interest are selected in the image of the skin sections and corresponding pixels in the white reference image are modeled using a gamma-distribution function. The resulting white reference signal is used to convert raw signal counts to percent reflectance. A schematic of this process is depicted in Figure 5.5, where the spectrums of the pixels selected in Figure 5.4 are normalized to percentage reflectance between $[0, 1]$.

It is evident that the normalized spectrums are extremely noisy in wavelength ranges below 450 nm and above 800 nm. Therefore, the spectrums are smoothened using a moving average filter, and a feasible region between 450 to 800 nm is chosen for all further analysis. While this is predominantly in the visible region of the electromagnetic spectrum, the high spectral resolution of the hyperspectral camera provides adequate information for analysis. The filtered spectrums for the same two pixels are shown in Figure 5.6, with the feasible region marked but dashed vertical lines.

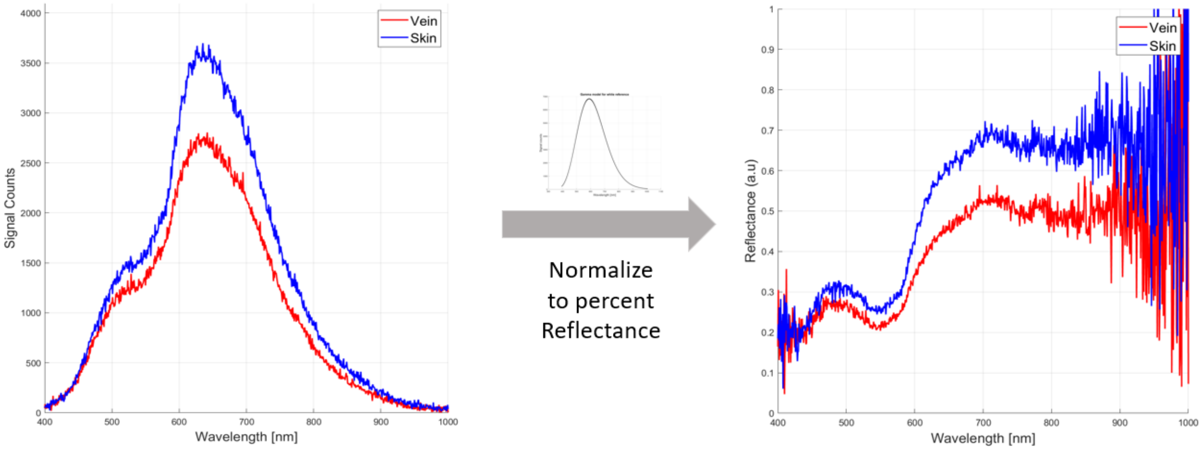

Figure 5.5: Conversion of raw spectrums to percentage reflectance. The raw spectrums of selected pixels are converted to percentage reflectance using the a gamma-distribution fit of the corresponding white reference pixel. The percentage reflectance values obtained from this conversion represents output/input in the system (skin). The reflectance obtained is very noisy, as seen in the plot on the right.

Spectrums from Set-1 in the regions of vein and skin are depicted in the next figure, Figure 5.7 for all four subjects. While all subjects in Set-1 are Caucasian, a significant difference in skin and vein spectrums is observed, especially with Subject-A. This could be due to the differences in melanin and blood volume fractions in the skin. These factors depend on a variety of reasons, such as lineage, diet, age, health conditions and activity levels. Furthermore, comparing spectrums from Set-2 corroborate the differences further, as Subject-E and Subject-F are of Southeast Asian descent, and have evidently more melanin. These spectrums are depicted in Figure 5.8. It is also observed that with an increase in melanin content, characteristic peaks in the spectrum in the wavelengths 450 – 550 nm, and 550 – 600 nm are suppressed. Similar features are noticed at higher wavelengths of 650 – 750 nm for Subject-E and Subject-F.

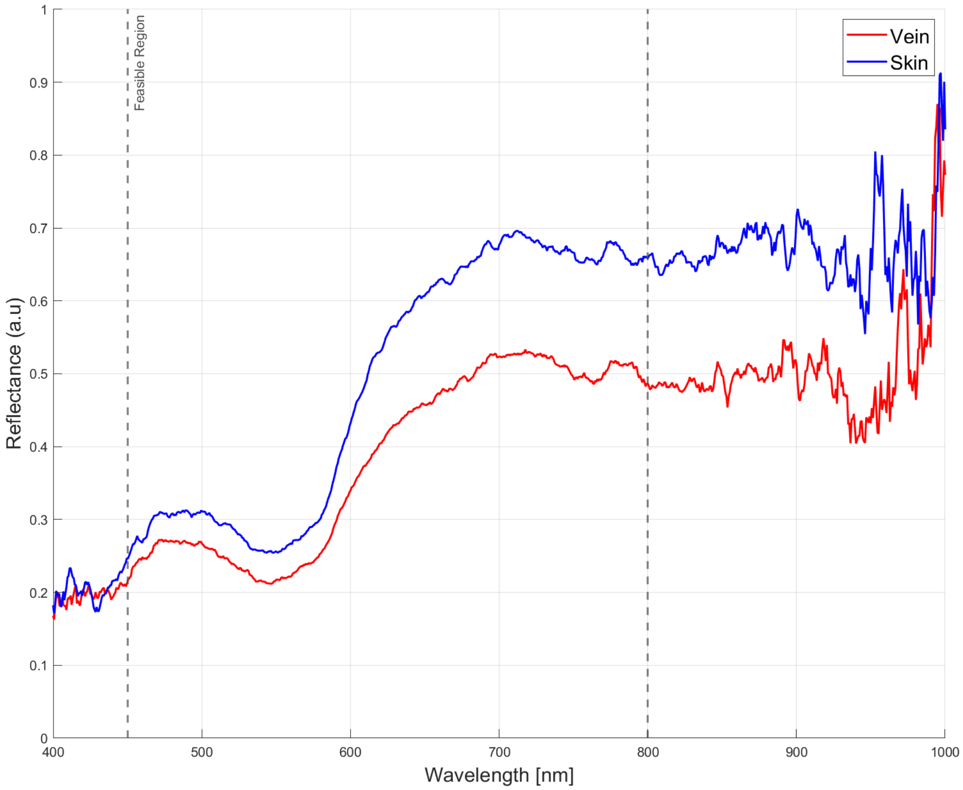

Figure 5.6: Filtered spectrum: A moving average filter was used to filter out high frequency noise from the percent reflectance spectrum. Then, the region of interest was chosen as 450 - 800 nm to avoid the spikes observed at higher wavelengths.

5.2 Sensitivity analysis of numerical model

An important step in validating the model is characterizing the input and output relationship in the theoretically model, especially since the numerical model described in Chapter 4 takes in multiple inputs to produce a single output. Additionally, all outputs are wavelength dependent as well, which adds another level of complexity to the system. Hence, a simple sensitivity analysis is carried out to establish bounds and relationships between the model's reflectance output and melanin, blood volume fraction and blood oxygen saturation. Sensitivity analysis refers to the process of identifying the influence of different sources of uncertainty in the input of a mathematical model on the outputs of the model. Sensitivity

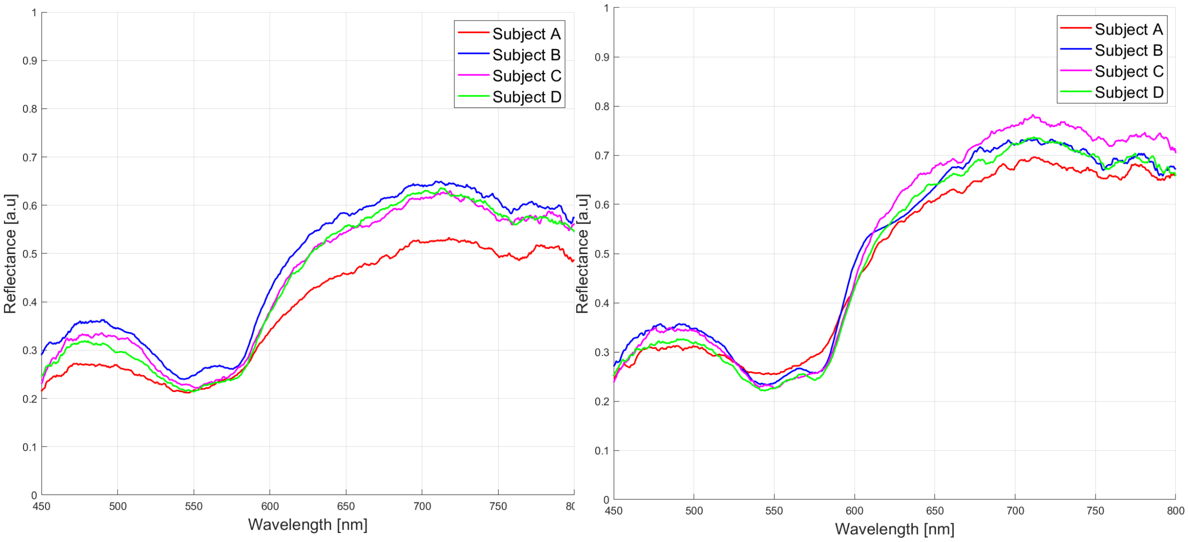

(a) Spectrum of pixels in venous regions (b) Spectrum of pixels in non-venous regions

Figure 5.7: Comparison of spectrums in Set-1. (a) shows spectrums of pixels selected in regions that clearly contain a vein and (b) shows spectrums of pixels selected from non-venous regions. A drop in magnitude in venous, especially for Subject A, was observed.

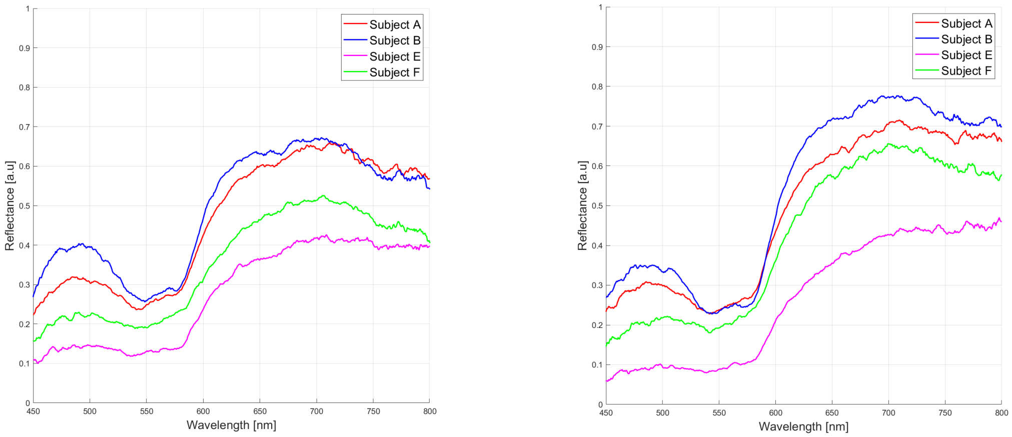

(a) Spectrum of pixels in venous regions (b) Spectrum of pixels in non-venous regions

Figure 5.8: Comparison of spectrums in Set-2. (a) shows spectrums of pixels selected in regions that clearly contain a vein and (b) shows spectrums of pixels selected from non-venous regions. Magnitude of reflectance spectrums from Subjects E and F are much lower than those of Subject A and B for both vein and skin regions.

analysis studies can aid removal of unnecessary inputs and eliminate redundant parameters in the model. The dimension of hyperspectral images in this thesis is enormous, with datasets having more than 100,000,000 data points in the X, Y, and λ dimensions combined. Even after pixels are selected and analyzed as a spectrum across the wavelength dimension, as done in Section 5.1, each pixel has a dimension of 487 wavelength bands.

In this thesis, the theoretical model of human skin reflectance has five inputs. These are the concentration of melanin, the blood volume fraction, blood oxygen saturation, and scattering coefficient parameters 'A' and 'B'. The model generates reflectance at every specified wavelength, given these five inputs at these wavelengths. It was found that scattering coefficient parameters 'A' and 'B' are highly correlated and must be dealt with separately. To match the high resolution of the measured data, the number of skin reflectance values generated are at 487 wavelengths, which proves to be computationally expensive. It would be beneficial from both a measurement and computational standpoint to efficiently isolate the wavelengths that are most responsive to variations in melanin, blood volume fraction and blood oxygen saturation.

To calculate the sensitivity of a model $f(x_1, x_2)$ with respect to the variable x_1, the model must be differentiated with respect to that parameter, which is described in Equation 5.1. However, due to the numerical nature of the model of the skin, the derivative of the reflectance must also be numerically derived. Furthermore, since both the reflectance as well as the absorption coefficient of melanin is a function of wavelength, the wavelengths at which change in melanin concentration results in maximum variation in numerical reflectance of the skin must be located. Studies show melanin in light-skinned humans such as Caucasians range from 1.3% to 6.3% [81]. Taking this into consideration, numerical reflectance is calculated across the feasible wavelength span of 450 – 800 nm while changing melanin concentration from 1% to 10%, with a step change of 1%. The resulting plot is shown in

Figure 5.9a. Since minimal change was observed, melanin concentration was varied from 10% to 100%, with a step change of 10%. Evidently, the resulting plot in Figure 5.9b shows that while melanin does not drastically change reflectance values, the characteristic dips observed at around 525 and 575 nm are flattened with the increase in melanin. This is similar to the findings in measured data, in Section 5.1 for subjects with higher melanin content.

$$S_{f,x_1} = \frac{df(x_1, x_2)}{dx_1} \tag{5.1}$$

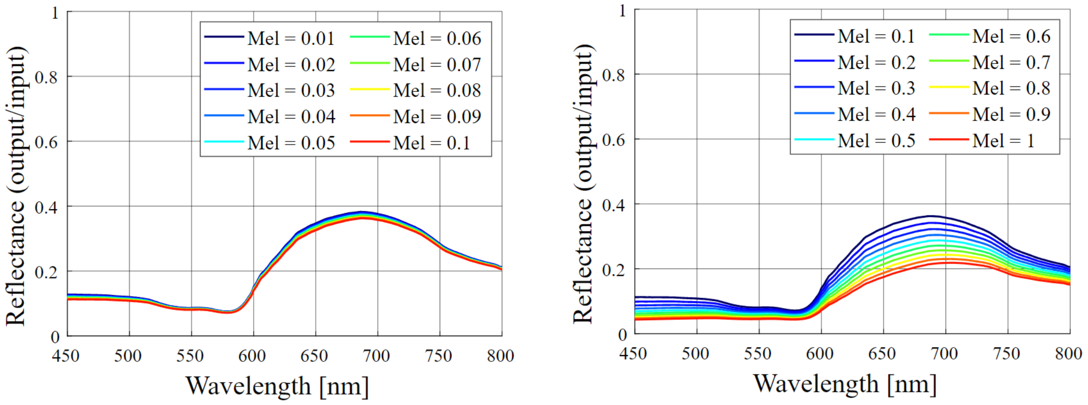

(a) Melanin content varying from 0.1 - 1% (b) Melanin content varying from 10 - 100%

Figure 5.9: Relationship of theoretical model to changes in melanin across feasible wavelength range 450 - 800 nm. The increase in melanin causes two major changes: decrease in magnitude of reflectance between 600 and 750 nm, and the supression of the two dips between 500 and 600 nm

To find the wavelengths that show most variations with respect to melanin, each curve in Figure (5.9b) is subtracted from the previous one, and divided with the change in melanin between each curve. This is mathematically described in Equation (5.2) as the numerical derivative of the reflectance at every wavelength with respect to melanin. The resulting plots of the numerical derivative of reflectance with respect to melanin are shown in Figure 5.10. The wavelengths that undergoes the most change is marked in each curve, which is 450 nm and 660 nm in the case of melanin.

$$S_{R,f_{mel}}(f_{mel}, f_{blood}, SpO2, \lambda) = \frac{R(f_{mel}^{i+1}, f_{blood}, SpO2, \lambda) - R(f_{mel}^{i}, f_{blood}, SpO2, \lambda)}{f_{mel}^{i+1} - f_{mel}^{i}} \tag{5.2}$$

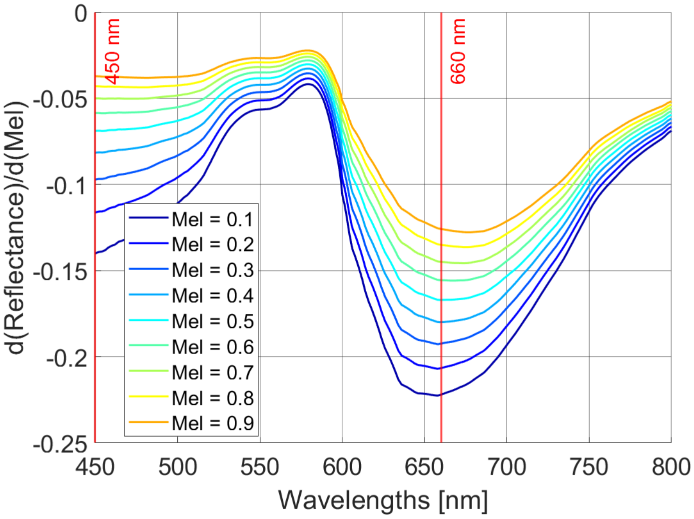

Figure 5.10: Senstivity of theoretical reflectance with respect to melanin in the feasible wavelength range 450 - 800 nm. The model is numerically differentiated with respect to melanin and the wavelengths with maximum change are marked in red.

Similarly, the numerical skin reflectance is analyzed with respect to blood volume fraction (BVF) and blood oxygen saturation (SpO2). The numerical sensitivity with respect to BVF and SpO2 is given in Equation 5.3 and Equation (5.4) respectively. In the case blood volume fraction, two ranges were picked to understand the influence of the variable on the model. These were 0.1% to 2% and 2% to 5%. For SpO2, studies show that blood oxygen values in venous blood are from 75% to 84%, while anything below 93% in arterial blood is considered hypoxia [82]. Keeping this mind, the range to analyze sensitivity of the model was determined to be from 70% to 100%. Figures depicting these sweeps for BVF are Figure 5.12, Figure

$$S_{R,f_{blood}}(f_{mel}, f_{blood}, SpO2, \lambda) = \frac{R(f_{mel}, f_{blood}^{i+1}, SpO2, \lambda) - R(f_{mel}, f_{blood}^{i}, SpO2, \lambda)}{f_{blood}^{i+1} - f_{blood}^{i}} \tag{5.3}$$

$$S_{R,SpO2}(f_{mel}, f_{blood}, SpO2, \lambda) = \frac{R(f_{mel}, f_{blood}, SpO2^{i+1}, \lambda) - R(f_{mel}, f_{blood}, SpO2^{i}, \lambda)}{SpO2^{i+1} - SpO2^{i}} \tag{5.4}$$

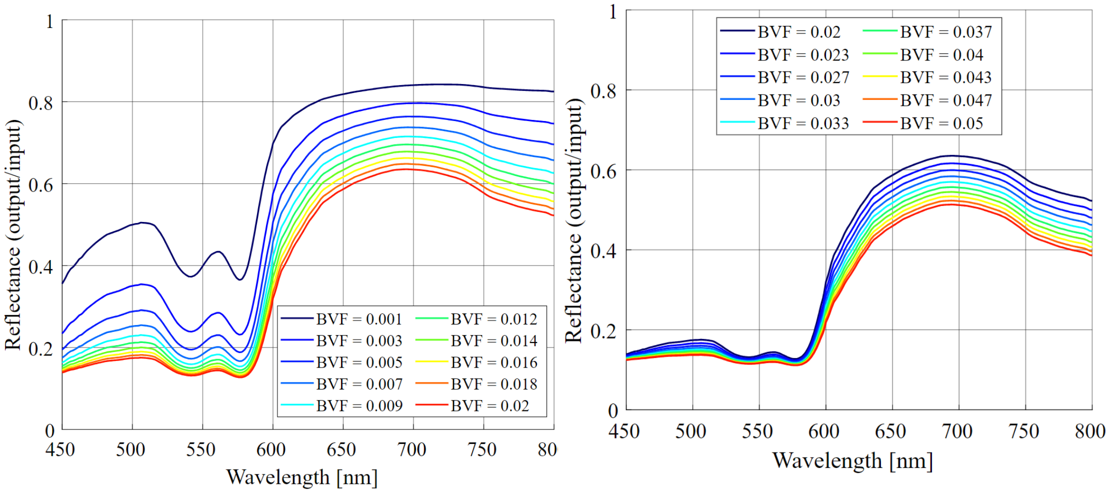

(a) BVF content varying from 0.1 - 2%

(b) BVF content varying from 2 - 5%

Figure 5.11: Relationship of theoretical model to changes in BVF across feasible wavelength range 450 - 800 nm. A large difference in spectral reflectance values is noticed when blood volume fraction is lowered. Therefore, the relationship between BVF and spectral reflectance is highly non-linear.

Wavelengths with the maximum variations with respect to change in blood volume fraction are regions around 500 to 520 nm and 590 to 625 nm, as seen in Figure 5.11. As blood volume fraction increases, the wavelengths of interest that are around 600 nm shift to longer wavelengths. On the contrary, the wavelengths of interest around 520 nm shift to shorter wavelengths with increase in blood volume fraction. Wavelengths between 750 - 800 nm also

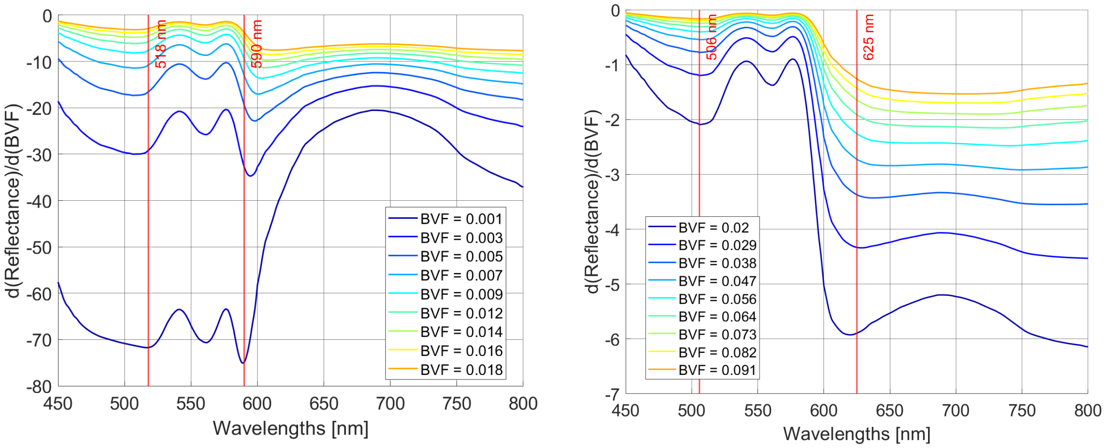

(a) BVF content varying from 0.1 - 2%

(b) BVF content varying from 2 - 5%

Figure 5.12: Senstivity of theoretical reflectance with respect to BVF in the feasible wavelength range 450 - 800 nm. Wavelengths at which spectral reflectances changes the most with respect to BVF are 506, 589 and 627 nm.

show significant variation with blood volume fraction, and can also be considered a band of interest. Similarly, Figure 5.13a, Figure 5.13b show that wavelengths 606, 646 and 750 nm are ideal to pick up changes in blood oxygen saturation. It is evident from these figures while melanin has little significant in the magnitude of reflectance, it plays a vital role in the characteristic shape of the curve. SpO2 contributes most significantly in the wavelength range 600 - 750 nm. The characteristic peaks between 500 - 600 nm can be attributed to blood volume fraction, which is supported by Nagaoka et al. [54]'s initial findings in calculating Erythema and Melanin indices. With a better understanding of the upper and lower bounds of the model, and it's sensitivity to uncertainty in the variables, the model can now be applied to the measured hyperspectral data for validation and extraction of characteristics features in the human skin.

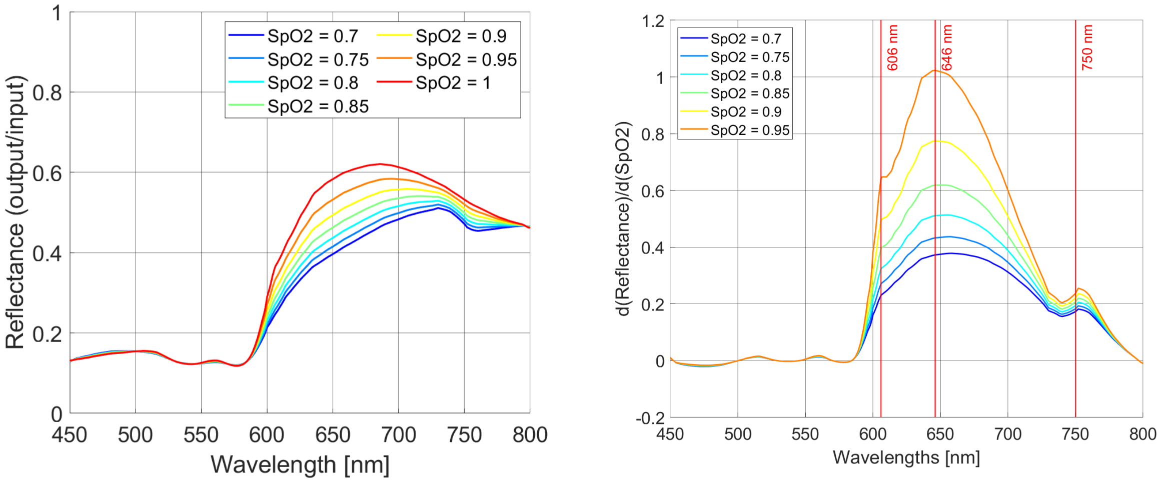

(a) SpO2 varying from 70 - 100%

(b) $S_{R,SpO2}$ for SpO2 varying from 70 - 100%

Figure 5.13: Relationship and senstivity of theoretical model to changes in SpO2 through 450 - 800 nm. Most change is noticed between 600 to 750 nm, with peaks in the sensitivity plot observed at 606, 646 and 750 nm

5.3 Results from model fit

In order to get insights about the model parameters explored in the previous section from measured data, the theoretical model of the reflectance of human skin must be fit to the measured hyperspectral data obtained in Secion 5.1. The outcomes from fitting the model to the data provide the basis for informed decision making about the state of the skin, the health of the skin, perfusion, and more.

This can be done by estimating the coefficients in the numerical model of the skin from the measured data. Since the model is clearly non-linear, the trust-region reflective algorithm is used to minimize the sum of squared residuals between the measured hyperspectral data and the model, as outlined in Chapter 4. Due to computational limitations, target pixels were selected across the entire image in regions of skin and vein. The three cases run for each subject were “only skin”, “only vein”, “skin and vein”, while trying to maximize the scatter across the picture. Figure 5.14 depicts the selected pixels in Subject-A and Subject-

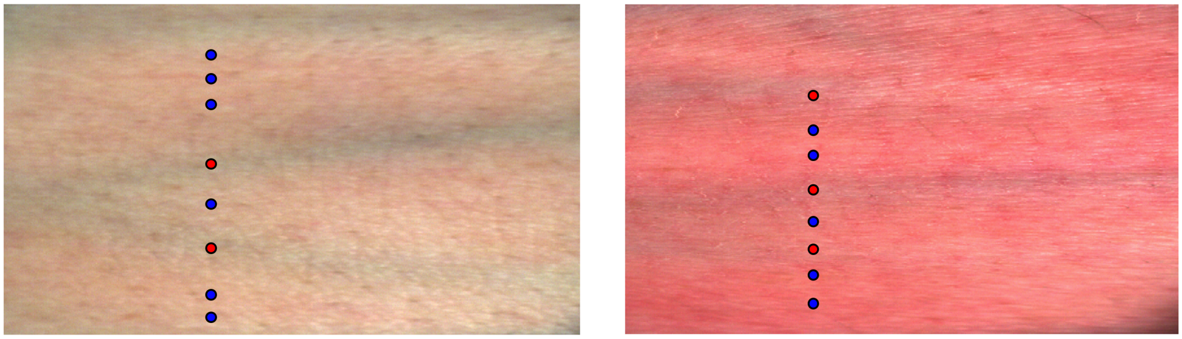

(a) Array of pixels in Subject-A (b) Array of pixels in Subject-B

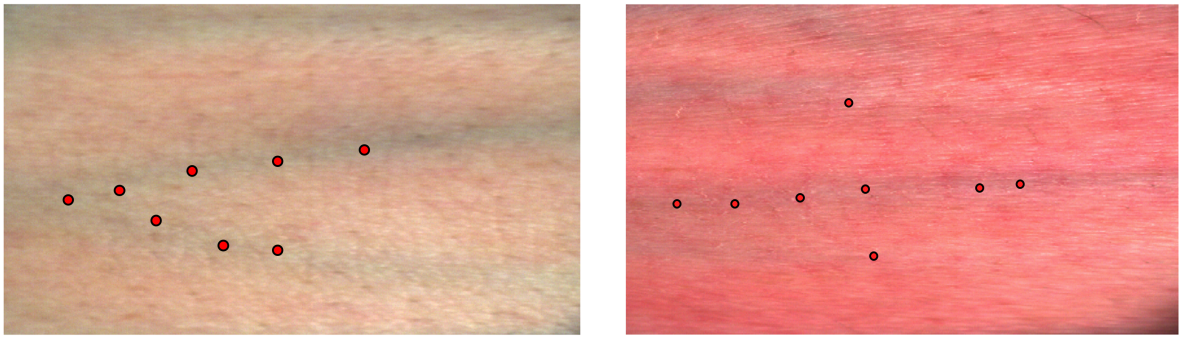

(c) Venous pixels in Subject-A (d) Venous pixels in Subject-B

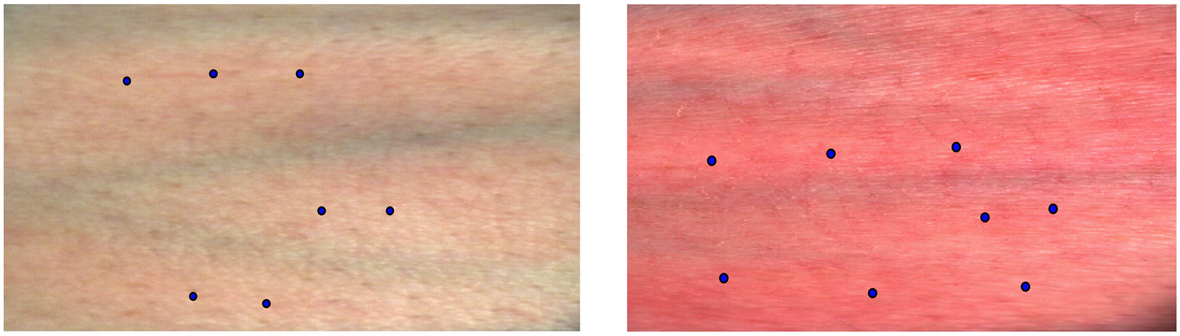

(e) Non-venous pixels in Subject-A (f) Non-venous pixels in Subject-B

Figure 5.14: Selected vein and skin pixels from Set-1. Pixels were selected in three cases: (a) and (b) in a line, passing through regions of veins and skins, (c) and (d) pixels in the venous regions, (e) and (f) pixels in skin regions.

B from Set-1. Subject-A has two pixels in venous regions while Subject-B has 3 pixels in venous regions. For all figures, pixels of venous regions are marked by red, while the pixels in non-venous regions are marked in blue.

The results from the minimization algorithm for a pixel in venous region and non-venous

		f_{mel}		f_{blood}		$SpO2$	
		Mean	STD	Mean	STD	Mean	STD
Subject A	Vein	0.059	1.3×10^{-9}	0.094	0.0093	0.803	0.029
	Skin	0.06	0	0.0017	0.00017	0.8	0
	Total	0.059	9.1×10^{-10}	0.0478	0.0471	0.801	0.02
Subject B	Vein	0.059	2.9×10^{-7}	0.0299	0.0089	0.77	0.026
	Skin	0.05	0.022	0.016	0.003	0.80	0.004
	Total	0.054	0.0166	0.022	0.0091	0.78	0.026

Table 5.1: Skin chromophores results from model fit of Set-1

regions for Subject-A and Subject-B in set-1 are shown in Figure 5.15 and Figure 5.16. The figures depict worst and best fits from the a total of 10 venous pixels and 13 non-venous pixels for Subject - A and 11 venous pixels and 13 non-venous pixels for Subject - B in Set - 1. The mean and standard deviations of each of the extracted variables, melanin content (f_{mel}), blood volume fraction (f_{blood}) and blood oxygen saturation ($SpO2$) are displayed in Table 5.1.

It is evident that in Set-1, the blood volume fraction of both subjects is higher for venous regions than non-venous regions, which can be intuitively explained since veins carry blood from different parts of the body to the heart. Veins in the dorsal portion of the hand are also superficial, in comparison to the radial arteries and dorsal digital arteries, which are buried deep in the muscle of the hand. Not much change in blood oxygen is observed when moving from venous regions to a region of the skin with no vein. There could be explained by a few reasons. The distance from which the camera images the skin could be too high to pick up the minute capillaries in the superficial layers of the skin. The resolution of the camera could be too low, giving us the same result. Furthermore, the lower-than-expected blood oxygen saturation could be due to the inhomogeneous distribution of capillaries in the skin, or the constriction of capillaries due to possible cold imaging conditions.

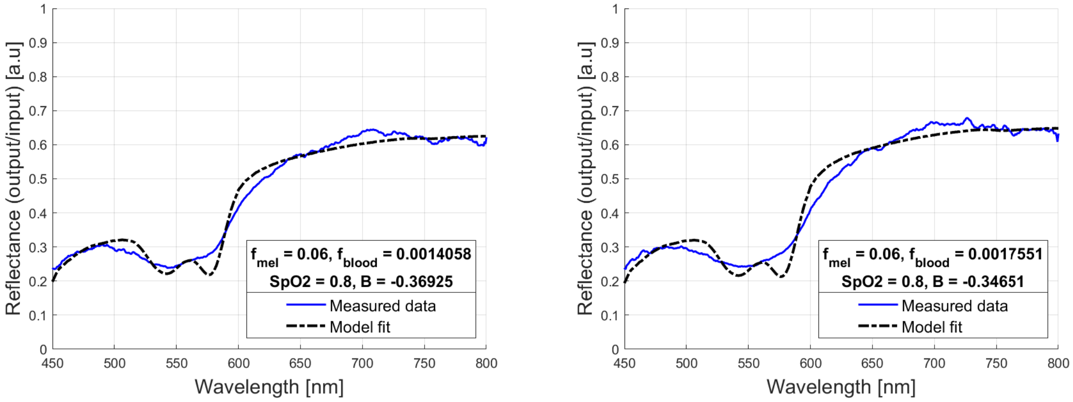

(a) Optimal fit for skin pixel (b) Least optimal fit for skin pixel

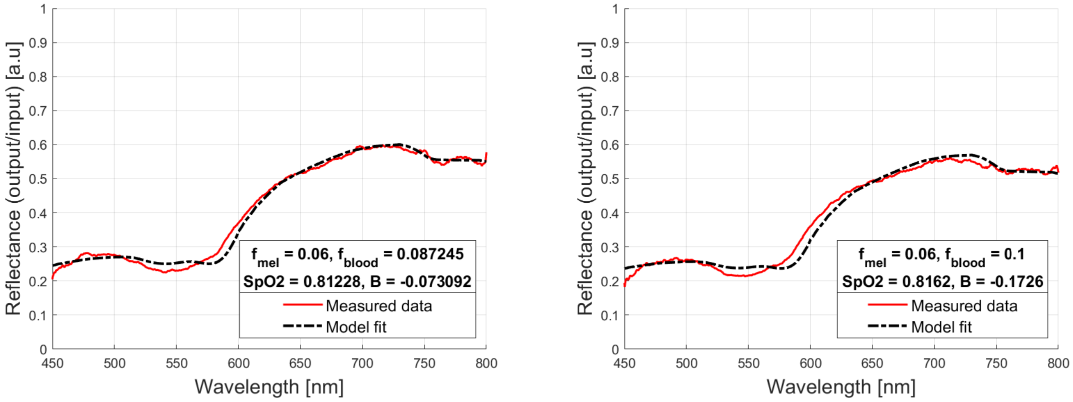

(c) Optimal fit for vein pixel (d) Least optimal fit for vein pixel

Figure 5.15: Comparison of best and worst fits in venous and skin pixels in Subject A. The sum of squared errors for the best and worst fits in the skin regions are 0.26 and 0.38 respectively. The sum of squared errors for best and worst in the vein regions are 0.1 and 0.15 respectively.

Similarly, pixels in the venous and non-venous regions were picked in images of Subject - A, Subject - B and Subject - F in Set - 2, as shown in Figure 5.17. At least 10 venous and 12 non-venous pixels were selected for each subject in Set - 1. Additionally, all subjects in Set-2 were requested to exert physical energy by lifting a heavy object a few minutes prior to imaging. It is a fundamental fact that any physical activity increases blood flow to the working tissues in order to provide the muscle with oxygen. Therefore, it can be expected that subjects in Set-2 have higher bloody oxygen values than those in Set-1, who had no

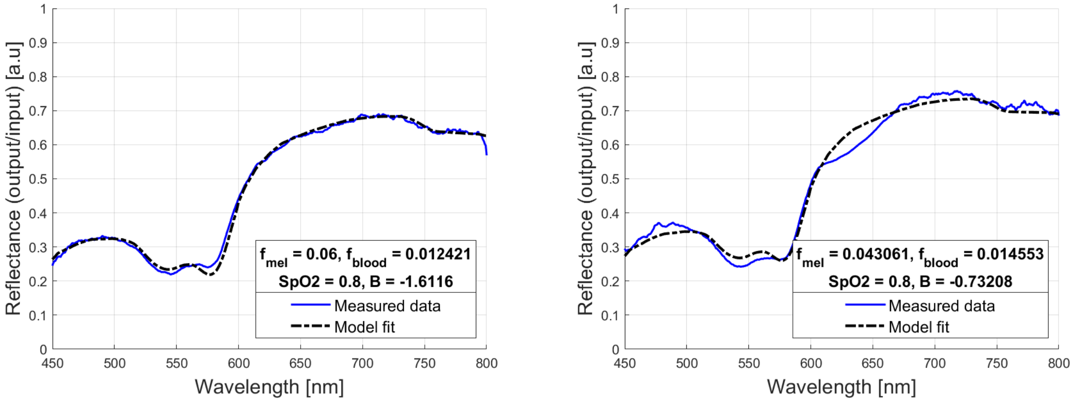

(a) Optimal fit for skin pixel (b) Least optimal fit for skin pixel

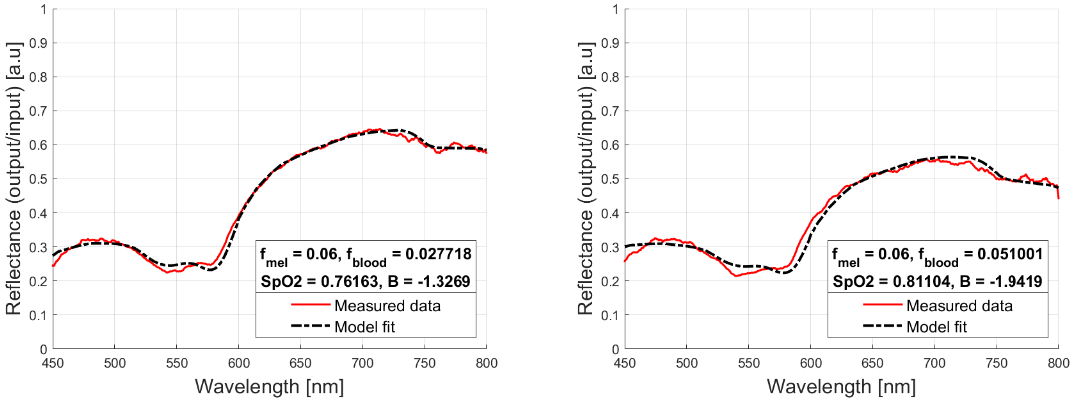

(c) Optimal fit for vein pixel (d) Least optimal fit for skin pixel

Figure 5.16: Comparison of best and worst fits in venous and skin pixels for Subject B. The sum of squared errors for the best and worst fits in the skin regions are 0.05 and 0.24 respectively. The sum of squared errors for best and worst fits in the vein regions are 0.07 and 0.145 respectively.

physical activity prior to imaging.

Such an outcome is evidently visible in the parameters listed in Table 5.2, especially for Subject - B. Average blood oxygen saturation values in the non-venous regions is 95%, certain pixels reporting a value of 99% as well. Further more, an increase in blood oxygen saturation for Subject - A and Subject - F was also found for the non-venous regions in comparison to the venous regions. This can be seen in Figure 5.18b for Subject-A and Figure 5.20b for Subject - F. The reason this increase in blood oxygen saturation estimation

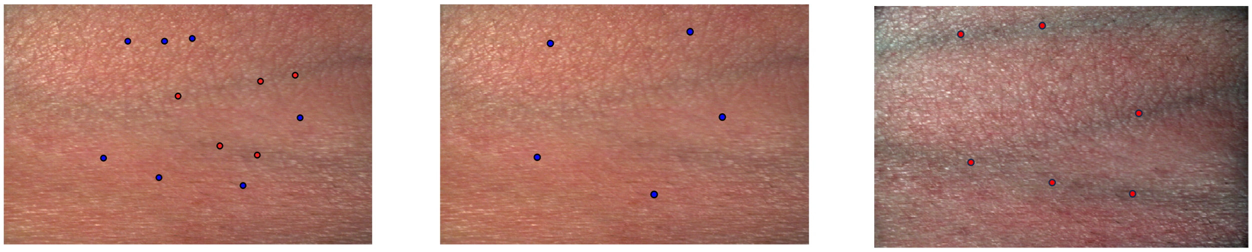

(a) Subject-A Set-2 Case 1 (b) Subject-A Set-2 Case 2 (c) Subject-A Set-2 Case 3

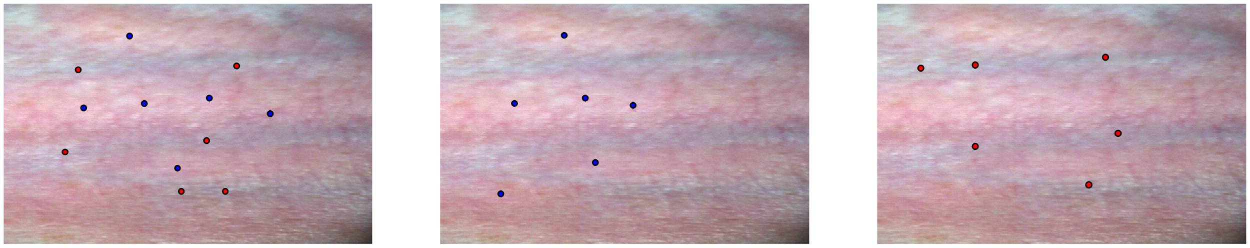

(d) Subject-B Set-2 Case 1 (e) Subject-B Set-2 Case 2 (f) Subject-B Set-2 Case 3

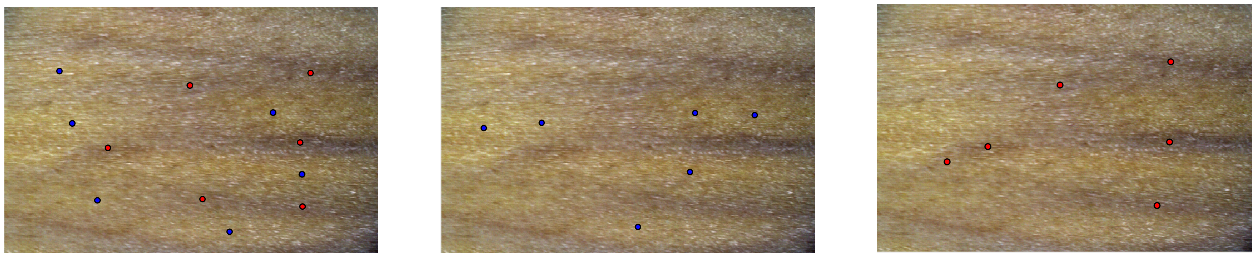

(g) Subject-F Set-2 Case 1 (h) Subject-F Set-2 Case 2 (i) Subject-F Set-2 Case 3

Figure 5.17: Selected vein and skin pixels from Set-2. Pixels were selected in three cases: (a), (b) and (c) for case 1, all across regions of veins and skins, (d), (e) and (f) for case 2, pixels in the venous regions, (g), (h) and (i) for case 3pixels in skin regions.

is most prominent in Subject - B could be due to the physical build of the subject. Subject - B can be considered to have a much lower body fat percentage that the other comparing subjects due to their regular visits to the gym, as well as their healthier diets. Additionally, the higher values of melanin in Subject - F greatly masks the influence of blood in the shorter wavelengths, making estimations unreliable for subjects of color.

		f_{mel}		f_{blood}		$SpO2$	
		Mean	STD	Mean	STD	Mean	STD
Subject A	Vein	0.064	0.0195	0.036	0.029	0.889	0.033
	Skin	0.069	2.2×10^{-8}	0.025	0.0065	0.895	0.0761
	Total	0.0672	0.013	0.03	0.02	0.892	0.059
Subject B	Vein	0.018	0.0275	0.0181	0.0169	0.799	0.063
	Skin	0.0066	0.019	0.015	0.003	0.95	0.092
	Total	0.0125	0.024	0.016	0.012	0.875	0.1
Subject F	Vein	0.39	0.022	0.0048	0.010	0.810	0.0617
	Skin	0.38	0.056	0.0138	0.0165	0.865	0.051
	Total	0.386	0.042	0.0093	0.0142	0.838	0.0622

Table 5.2: Skin chromophores results from model fit of Set-1

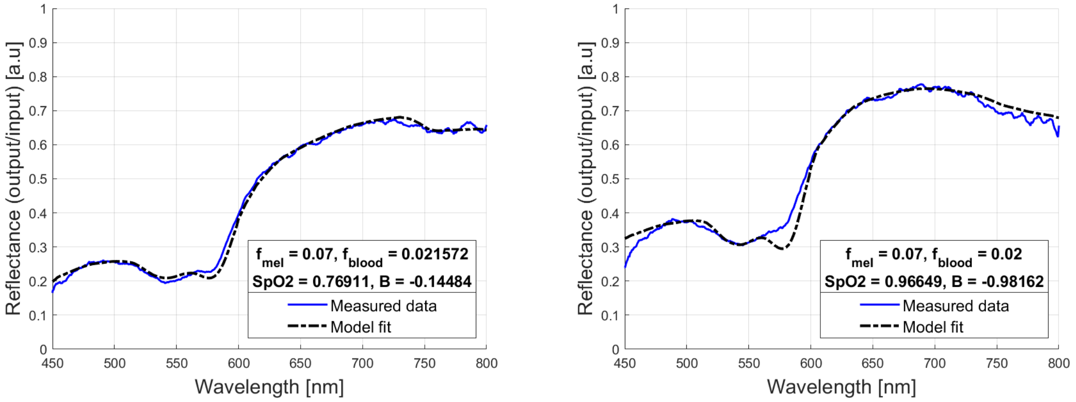

(a) Optimal fit for skin pixel (b) Least optimal fit for skin pixel

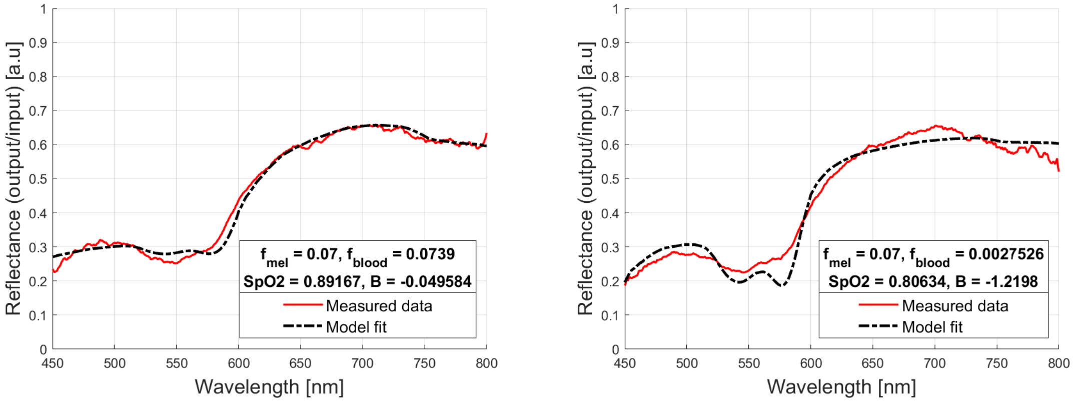

(c) Optimal fit for vein pixel (d) Least optimal fit for skin pixel

Figure 5.18: Comparison of best and worst fits in venous and skin pixels for Subject A in Set-2. The sum of squared errors for the best and worst fits in the skin regions are 0.07 and 0.29 respectively. The sum of squared errors for optimal and least optimal fits in the vein regions are 0.14 and 0.46 respectively.

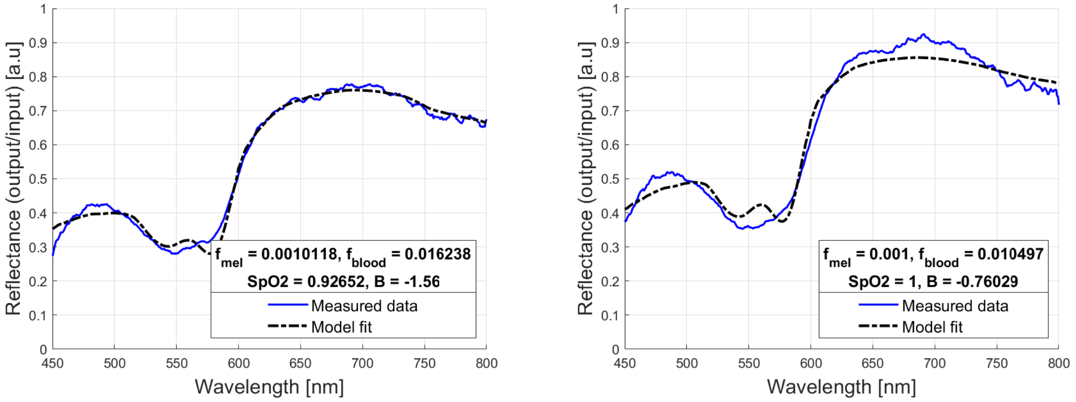

(a) Optimal fit for skin pixel (b) Least optimal fit for skin pixel

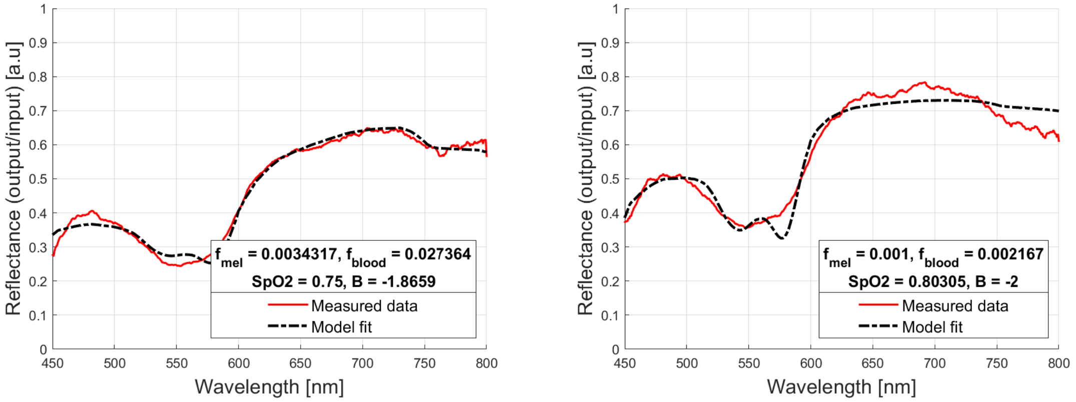

(c) Optimal fit for vein pixel (d) Least optimal fit for vein pixel

Figure 5.19: Comparison of best and worst fits in venous and skin pixels for Subject B in Set-2. The sum of squared errors for the best and worst fits in the skin regions are 0.15 and 0.54 respectively. The sum of squared errors for optimal and least optimal fits in the vein regions are 0.15 and 0.55 respectively.

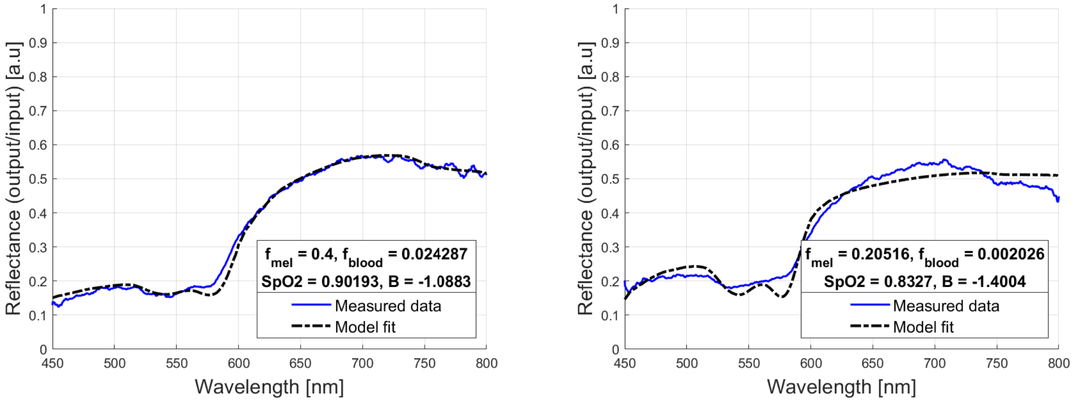

(a) Optimal fit for skin pixel (b) Lease optimal fit for skin pixel

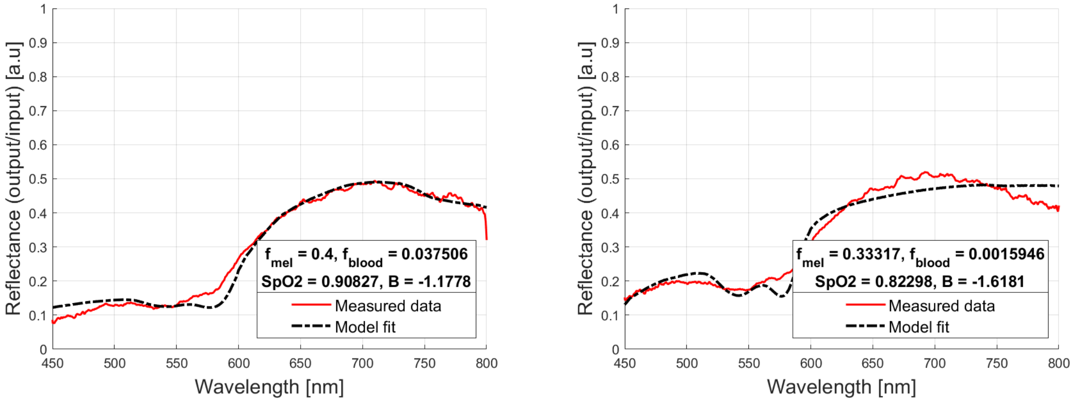

(c) Optimal fit for vein pixel (d) Least optimal fit for vein pixel

Figure 5.20: Comparison of best and worst fits in venous and skin pixels for Subject F in Set-2. The sum of squared errors for the best and worst fits in the skin regions are 0.099 and 0.34 respectively. The sum of squared errors for optimal and least optimal fits in the vein regions are 0.3 and 0.4 respectively.

5.4 Summary

In summary, this chapter discusses in detail the spectral data obtained from hyperspectral imaging of the skin. Each pixel contains extensive information, and one of the main objectives of this study is to extract meaningful and interpretable information from this dataset. The model discussed in Chapter 4, based on the Kubelka-Munk Theory and the Beer-Lambert-Bouguer law is analyzed for its sensitivity to variations in various inputs. Additionally, since the model is a function of wavelength, the wavelengths at which the model exhibited highest response were identified to be 450 and 660 nm for melanin, 500 - 520 nm and 590 - 625 nm for blood volume fraction and 606, 646 and 750 nm for blood oxygen saturation. Subsequently, the model was applied to fit the hyperspectral data obtained from selected pixels for a variety of subjects. A significant increase in blood oxygen saturation was observed when comparing images in Set-1 and Set-2, since the latter were captured after subjects performed some physical activity. Additionally, the influence of melanin in both the model and the measured data was found to exhibit similar patterns. These findings contribute to a better understanding of the relationship between skin characteristics and spectral data and highlights the importance of specific wavelengths for future investigations.

Chapter 6

Conclusions

As the final chapter of this thesis, this chapter summarizes the findings of the study and sheds light on potential points for future research. The goal of this study is to explore the application of Hyperspectral imaging in the biomedical field as a means to distinguish between healthy skin and melanoma skin lesions. Melanomas and typical unhealthy skin lesions have characteristic shapes, melanin and blood patterns and variations in water content. Hyperspectral imaging can be a powerful tool in analyzing these skin lesions, as it enables the capture of back-scattered intensities across a continuous spectrum beyond the capabilities of the human eye or standard digital cameras.

Hyperspectral images of human skin are a composite of numerous elements in the skin. The skin is a turbid, inhomogeneous material, that has chromophores and scattering agents. As light enters the skin, it changes due to these agents. The back-scattered light from the skin is picked up by the hyperspectral camera in the visible and near-infrared (VNIR) regions. The output images consist almost exclusively of impure pixels – pixel intensities that are a result of a combination of scattering and absorption components, and not a result of a homogenous material. Ultimately, the pixels must be converted into meaningful physical characteristics of the skin for the data to have diagnostic significance.

To explore this hypothesis, numerous hyperspectral images of human skin on the dorsal portion of the hand were taken in this study. The images were taken in two sets, where Set–1 contained four adult Caucasian males and Set–2 contained two Caucasian males and two

Southeast Asian males. A well-known mathematical approach found in literature is using the Kubelka-Munk theory to model human skin as a bi-layer planar system. A similar approach, in conjunction with the laws of Beer-Lamber-Bouguer for attenuation in materials, is applied to obtain physical characteristics of the human skin from the hyperspectral images. These physical characteristics include melanin, blood volume fraction and blood oxygen saturation. During the course of this study, the outcomes obtained do not entirely correspond to the original mission statement. The main motivation of the study was to establish grounds for assistive diagnostic techniques in detecting melanomas and differentiating between healthy and unhealthy skin. However, in the process of implementing a methodology to achieve this goal, a number of unexpected problems and points of contentions revealed themselves. The process of calibrating the camera and ensuring that the images acquired were appropriately converted into physical measurements was crucial to the progress of the project. Additionally, to validate the model as an suitable representation of the physical interactions between light and the human skin, it was necessary to understand the variations in the model's output reflectance with the inputs (blood volume fraction, blood oxygen saturation and melanin content). Therefore, this the contributions of this thesis morphed into a preliminary study focused on establishing a robust calibration process for image acquisition and identifying the major sources of variation in both image acquisition and modeling of the skin. To calibrate and convert raw hyperspectral images into percentage reflectance, white reference and dark current frames were acquired. The calibration process described in the study compensates for the hyperspectral camera's incapability to capture the capture the characteristics of the illuminating light as well as the white reference using a gamma-distribution model. The enabled the use of a low-cost white reference to normalize the hyperspectral images to percentage reflectance. In almost all these pictures, distinct outlines of venous regions were observed, especially at longer wavelengths. Furthermore, a difference in overall images was observed when frames of shorter wavelengths were compared with longer wavelengths. The spectral characteristics observed within the VNIR regions, specifically ranging from 450 – 800 nm, indicate a discernable distinction in how incident light interacts with venous and non-venous regions in the skin.

The model is also analyzed for its sensitivity to uncertainty in these variables. Due to the wavelength-dependent nature of the hyperspectral data and each of these variables, the mathematical model was analyzed in terms of wavelength. It was found that 5 definite wavelengths 2 wavelength groups are most directly responsive to changes in the variables. These are 450 and 660 nm for melanin, 500 - 520 nm and 590 - 625 nm for blood volume fraction and 606, 646 and 750 nm for blood oxygen saturation. When the model was made to fit measured hyperspectral data using a non-linear least squares method, the average sum of squared residuals across all fits was found to be 0.22. Furthermore, a significant increase in blood oxygen saturation was observed when comparing images in Set-1 and Set-2 due to an increase in physical exertion in the latter. These results support the validation of the mathematical model. However, melanin content across the subjects significantly impacted the estimation of the other values.

6.1 Future work

The results discussed in this thesis serve as initial findings. The overarching objective of this research endeavour is to employ a combination of a physics-based model and a machine-learning algorithm to enable informed decision-making regarding healthy and unhealthy tissue, specifically concerning melanomas. It is evident that while the mathematical model outlined in this thesis effectively captures the physical behaviour, it falls short in identifying certain characteristics present in the measured signals. One such feature is the presence of two peaks in between 500 – 600 nm range. Although the model exhibits more pronounced dips than the measured data, it fails to accurately represent variation in the curve, across the different subjects. Additionally, the model does not adequately account for the small features at higher wavelengths.

The influence of melanin content is another aspect that needs to be further understood. Due to its higher absorption values at short wavelengths, melanin content plays a role in smoothening out the peaks and dips made by the blood volume fraction and blood oxygen saturation between 450 – 600 nm. However, the model consistently overestimated the melanin content for all subjects. This higher estimation of melanin content interferes with the accurate estimation of the other parameters, especially for subjects with higher melanin content in their skin. It is crucial to further investigate this issue in order to ensure that the methodology is inclusive of people of color, which is an important objective of this study. It is worth noting that pulse-oximetry has faced similar challenges, as occult hypoxemia in Black patients went undetected three times more frequent that in white patients [83]. Recently, modifications are being explored in pulse-oximetry, such as incorporating a white LED alongside the infrared, green and red LEDs to account for melanin content [84].

In this thesis, a few wavelengths were identified where the model was most sensitive to variations in the input parameters. However, in this process, all variables were treated to be independent. This is inaccurate, and blood volume fraction and blood oxygen levels are highly correlated variables. As a way to enhance the credibility of the results, a variance-based sensitivity analysis method that considers the correlations between parameters can be explored. Moving on to the measurement side, when dealing with large amounts of measured data, principal component analysis (PCA) is used to reduce the dimension and identify components that contribute the most variance in the data. However, PCA alone may not be the most suitable approach, as the resulting components lack physical significance. It might be worth exploring an alternative approach that combines PCA with the outcomes of the sensitivity analysis. This could potentially lead to a transition from the current high-fidelity model with nearly 500 wavelengths captured and modelled, to a low-fidelity model, offering improved computational efficiency with minimal loss in accuracy. Additionally, this approach could potentially replace the need for a complex hyperspectral imaging setup. Instead, a basic setup consisting of a high-quality digital camera and an array of LEDs emitting energy at the selected wavelengths can be used for efficient multi-spectral imaging.

Finally, the complexity of the imaging setup itself poses some challenges in interpreting the results. Due to an incapability to hold variables constant during experimental procedure, it's unclear whether the measured data amongst the different subjects varies due to differences in their inherent properties, or whether it is merely experimental error. The possible unaccounted variables in between subjects could be body temperature, time of day, activity level, lifestyle, diet, and health conditions. The sensor itself could have introduced these variances in the data. To address these challenges, better experimental design and a more robust statistical analysis of the data must be conducted. Moreover, due to the number of variables within the skin and in the experiment, multi-variate analysis techniques can be explored to understand the effects of different variables on the measured data and the model. Significance tests on the measured data to identify the differences between subjects within a set and between two sets of data can help understand the uncertainty in the system.

Bibliography

[1] Spectral senstivity. URL `https://en.wikipedia.org/wiki/Spectral_sensitivity`. Accessed: 2023-07-21.

[2] Composition of rgb from three grayscale images. URL `https://en.wikipedia.org/wiki/Grayscale#/media/File:Beyoglu_4671_tricolor.png`. Accessed: 2023-07-21.

[3] Hyperspectral imaging of process water. URL `https://hydroptics.eu/hyperspectral-imaging-of-process-water/`. Accessed: 2023-07-21.

[4] Thermal radiation. URL `https://seos-project.eu/earthspectra/earthspectra-c02-p12.html`. Accessed: 2023-07-21.

[5] Calculating the emission spectra from common light sources, . URL `https://www.comsol.com/blogs/calculating-the-emission-spectra-from-common-light-sources/`. Accessed: 2023-07-21.

[6] Nick Knighton and Bruce Bugbee. A mixture of barium sulfate and white paint is a low-cost substitute reflectance standard for spectralon®. *Tech Instrum*, 11:4–6, 2005.

[7] Layers of the skin. URL `https://my.clevelandclinic.org/-/scassets/images/org/health/articles/21902-hypodermis`. Accessed: 2023-07-21.

[8] Marc Clement, Gwenaelle Daniel, and Mario Trelles. Optimising the design of a broad-band light source for the treatment of skin. *Journal of Cosmetic and Laser Therapy*, 7 (3-4):177–189, 2005.

[9] Alexey N Bashkatov, E A Genina, V I Kochubey, and VV Tuchin. Optical properties of human skin, subcutaneous and mucous tissues in the wavelength range from 400 to 2000 nm. *Journal of Physics D: Applied Physics*, 38(15):2543, 2005.

[10] Paul C Lauterbur. Image formation by induced local interactions: examples employing nuclear magnetic resonance. *nature*, 242(5394):190–191, 1973.

[11] Wilhelm Conrad Röntgen. On a new kind of rays. *Science*, 3(59):227–231, 1896.

[12] Gabor T Herman. *Fundamentals of computerized tomography: image reconstruction from projections*. Springer Science & Business Media, 2009.

[13] Lars O Svaasand. Optics of tissue. In *Dosimetry of laser radiation in medicine and biology*, volume 10305, pages 115–133. SPIE, 1989.

[14] Andrew M Smith, Michael C Mancini, and Shuming Nie. Second window for in vivo imaging. *Nature nanotechnology*, 4(11):710–711, 2009.

[15] Paul Muller. Glossary of terms used in physical organic chemistry (iupac recommendations 1994). *Pure and Applied Chemistry*, 66(5):1077–1184, 1994.

[16] Takuo Aoyagi. Pulse oximetry: its invention, theory, and future. *Journal of anesthesia*, 17:259–266, 2003.

[17] Chein-I Chang. *Hyperspectral imaging: techniques for spectral detection and classification*, volume 1. Springer Science & Business Media, 2003.

[18] Michael W Levine and Jeremy M Shefner. Fundamentals of sensation and perception. 1991.

[19] Robert O Green, Michael L Eastwood, Charles M Sarture, Thomas G Chrien, Mikael Aronsson, Bruce J Chippendale, Jessica A Faust, Betina E Pavri, Christopher J Chovit,

Manuel Solis, et al. Imaging spectroscopy and the airborne visible/infrared imaging spectrometer (aviris). *Remote sensing of environment*, 65(3):227–248, 1998.

[20] Alexander FH Goetz, Gregg Vane, Jerry E Solomon, and Barrett N Rock. Imaging spectrometry for earth remote sensing. *science*, 228(4704):1147–1153, 1985.

[21] Bosoon Park and Renfu Lu. *Hyperspectral imaging technology in food and agriculture*, volume 1. Springer, 2015.

[22] Jian-hu Wu, Yan-kun Peng, Jing-jing Chen, Wei Wang, Xiao-dong Gao, Hui Huang, et al. Study of spatially resolved hyperspectral scattering images for assessing beef quality characteristics. *Spectroscopy and Spectral Analysis*, 30(7):1815–1819, 2010.

[23] Di Wu, Da-Wen Sun, and Yong He. Application of long-wave near infrared hyperspectral imaging for measurement of color distribution in salmon fillet. *Innovative Food Science & Emerging Technologies*, 16:361–372, 2012. ISSN 1466-8564. doi: https://doi.org/10.1016/j.ifset.2012.08.003. URL https://www.sciencedirect.com/science/article/pii/S1466856412001087.

[24] Delia Lorente, Nuria Aleixos, JUAN Gómez-Sanchis, Sergio Cubero, OSCAR LEONARDO García-Navarrete, and José Blasco. Recent advances and applications of hyperspectral imaging for fruit and vegetable quality assessment. *Food and Bioprocess Technology*, 5:1121–1142, 2012.

[25] Chandra B Singh, Digvir S Jayas, Jitendra Paliwal, and Noel DG White. Identification of insect-damaged wheat kernels using short-wave near-infrared hyperspectral and digital colour imaging. *Computers and electronics in agriculture*, 73(2):118–125, 2010.

[26] Di Wu and Da-Wen Sun. Advanced applications of hyperspectral imaging technology

for food quality and safety analysis and assessment: A review—part ii: Applications. *Innovative Food Science & Emerging Technologies*, 19:15–28, 2013.

[27] Guolan Lu and Baowei Fei. Medical hyperspectral imaging: a review. *Journal of biomedical optics*, 19(1):010901–010901, 2014.

[28] Jason A Chin, Edward C Wang, and Melina R Kibbe. Evaluation of hyperspectral technology for assessing the presence and severity of peripheral artery disease. *Journal of vascular surgery*, 54(6):1679–1688, 2011.

[29] Aksone Nouvong, Byron Hoogwerf, Emile Mohler, Brian Davis, Azita Tajaddini, and Elizabeth Medenilla. Evaluation of diabetic foot ulcer healing with hyperspectral imaging of oxyhemoglobin and deoxyhemoglobin. *Diabetes care*, 32(11):2056–2061, 2009.

[30] Martin Halicek, Himar Fabelo, Samuel Ortega, Gustavo M Callico, and Baowei Fei. In-vivo and ex-vivo tissue analysis through hyperspectral imaging techniques: revealing the invisible features of cancer. *Cancers*, 11(6):756, 2019.

[31] Bahram Khoobehi, James M Beach, and Hiroyuki Kawano. Hyperspectral imaging for measurement of oxygen saturation in the optic nerve head. *Investigative ophthalmology & visual science*, 45(5):1464–1472, 2004.

[32] Daniel S Gareau, Joel Correa da Rosa, Sarah Yagerman, John A Carucci, Nicholas Gulati, Ferran Hueto, Jennifer L DeFazio, Mayte Suárez-Fariñas, Ashfaq Marghoob, and James G Krueger. Digital imaging biomarkers feed machine learning for melanoma screening. *Experimental dermatology*, 26(7):615–618, 2017.

[33] Skin cancer 101, . URL `https://www.skincancer.org/skin-cancer-information/`. Accessed: 2023-07-21.

[34] Melanoma. URL https://www.aad.org/media/stats-melanoma. Accessed: 2023-07-17.

[35] Skin cancer facts & statistics, . URL https://www.skincancer.org/skin-cancer-information/skin-cancer-facts/#ethnicity. Accessed: 2023-07-21.

[36] Radiation: Ultraviolet (uv) radiation and skin cancer. URL https://www.who.int/news-room/questions-and-answers/item/radiation-ultraviolet-(uv)-radiation-and-skin-cancer. Accessed: 2023-07-17.

[37] Giuseppe Argenziano and H Peter Soyer. Dermoscopy of pigmented skin lesions–a valuable tool for early. *The lancet oncology*, 2(7):443–449, 2001.

[38] Many pathologists agree overdiagnosis of skin cancer happens, but don't change diagnosis behavior. URL https://www.washington.edu/news/2022/05/03/many-pathologists-agree-overdiagnosis-of-skin-cancer-happens-but-dont-change-diagno Accessed: 2023-07-21.

[39] Robert J Friedman, Dina Gutkowicz-Krusin, Michele J Farber, Melanie Warycha, Lori Schneider-Kels, Nicole Papastathis, Martin C Mihm, Paul Googe, Roy King, Victor G Prieto, et al. The diagnostic performance of expert dermoscopists vs a computer-vision system on small-diameter melanomas. *Archives of dermatology*, 144(4):476–482, 2008.

[40] Thomas Haugland Johansen, Kajsa Møllersen, Samuel Ortega, Himar Fabelo, Aday Garcia, Gustavo M Callico, and Fred Godtliebsen. Recent advances in hyperspectral imaging for melanoma detection. *Wiley Interdisciplinary Reviews: Computational Statistics*, 12 (1):e1465, 2020.

[41] Hans Grahn and Paul Geladi. *Techniques and applications of hyperspectral image analysis*. John Wiley & Sons, 2007.

[42] Notes on the resolution and other details of the human eye. URL https://clarkvision.com/articles/eye-resolution.html. Accessed: 2023-07-21.

[43] JK Bowmaker, HJ Dartnall, and JD Mollon. Microspectrophotometric demonstration of four classes of photoreceptor in an old world primate, macaca fascicularis. *The Journal of physiology*, 298(1):131–143, 1980.

[44] Junichi Nakamura. *Image sensors and signal processing for digital still cameras*. CRC press, 2017.

[45] Gregg Vane, Robert O Green, Thomas G Chrien, Harry T Enmark, Earl G Hansen, and Wallace M Porter. The airborne visible/infrared imaging spectrometer (aviris). *Remote Sensing of Environment*, 44(2):127–143, 1993. ISSN 0034-4257. doi: https://doi.org/10.1016/0034-4257(93)90012-M. URL https://www.sciencedirect.com/science/article/pii/003442579390012M. Airbone Imaging Spectrometry.

[46] xispec2 hyperspectral cameras. URL https://www.ximea.com/files/brochures/xiSpec-Hyperspectral-cameras-2015-brochure.pdf. Accessed: 2023-07-21.

[47] Nathan Hagen and Michael W Kudenov. Review of snapshot spectral imaging technologies. *Optical Engineering*, 52(9):090901–090901, 2013.

[48] Katharine L Hanlon, Grace Wei, Lilia Correa-Selm, and James M Grichnik. Dermoscopy and skin imaging light sources: a comparison and review of spectral power distribution and color consistency. *Journal of biomedical optics*, 27(8):080902–080902, 2022.

[49] Dermalite pigmentboost. URL https://dermlite.com/pages/pigmentboost. Accessed: 2023-07-21.

[50] M.E. Vestergaard, P. Macaskill, P.E. Holt, and S.W. Menzies. Dermoscopy compared with naked eye examination for the diagnosis of primary melanoma: a meta-analysis of studies performed in a clinical setting. *British Journal of Dermatology*, 159(3):669–676, 09 2008. ISSN 0007-0963. doi: 10.1111/j.1365-2133.2008.08713.x. URL `https://doi.org/10.1111/j.1365-2133.2008.08713.x`.

[51] Nikiforos Kollias. The physical basis of skin color and its evaluation. *Clinics in dermatology*, 13(4):361–367, 1995.

[52] Chein-I Chang and Antonio Plaza. A fast iterative algorithm for implementation of pixel purity index. *IEEE Geoscience and Remote Sensing Letters*, 3(1):63–67, 2006.

[53] Michael E Winter. N-findr: An algorithm for fast autonomous spectral end-member determination in hyperspectral data. In *Imaging Spectrometry V*, volume 3753, pages 266–275. SPIE, 1999.

[54] Takashi Nagaoka, Natalja S Eikje, Atsushi Nakamura, Katsuo Aizawa, Yoshio Kiyohara, Fumihiko Ichikawa, Toshio Yamazaki, Masao Doi, Katsushige Nakamura, Shinya Otsubo, et al. Inspection of skin hemodynamics with hyperspectral camera. In *2007 29th Annual International Conference of the IEEE Engineering in Medicine and Biology Society*, pages 3357–3361. IEEE, 2007.

[55] LE Dolotov, Yu P Sinichkin, VV Tuchin, SR Utz, GB Altshuler, and IV Yaroslavsky. Design and evaluation of a novel portable erythema-melanin-meter. *Lasers in Surgery and Medicine*, 34(2):127–135, 2004.

[56] Paul Kubelka and Franz Munk. An article on optics of paint layers. *Z. Tech. Phys*, 12 (593-601):259–274, 1931.

[57] Evgeny Zherebtsov, Viktor Dremin, Alexey Popov, Alexander Doronin, Daria Kurakina,

Mikhail Kirillin, Igor Meglinski, and Alexander Bykov. Hyperspectral imaging of human skin aided by artificial neural networks. *Biomedical optics express*, 10(7):3545–3559, 2019.

[58] Alexander Doronin and Igor Meglinski. Online object oriented monte carlo computational tool for the needs of biomedical optics. *Biomedical optics express*, 2(9):2461–2469, 2011.

[59] Dmitry Yudovsky and Laurent Pilon. Simple and accurate expressions for diffuse reflectance of semi-infinite and two-layer absorbing and scattering media. *Applied optics*, 48(35):6670–6683, 2009.

[60] Dmitry Yudovsky and Laurent Pilon. Rapid and accurate estimation of blood saturation, melanin content, and epidermis thickness from spectral diffuse reflectance. *Applied optics*, 49(10):1707–1719, 2010.

[61] Dmitry Yudovsky, Aksone Nouvong, and Laurent Pilon. Hyperspectral imaging in diabetic foot wound care. *Journal of diabetes science and technology*, 4(5):1099–1113, 2010.

[62] Lou Gevaux, Jordan Gierschendorf, Juliette Rengot, Marie Cherel, Pierre Séroul, Alex Nkengne, Julie Robic, Alain Trémeau, and Mathieu Hébert. Real-time skin chromophore estimation from hyperspectral images using a neural network. *Skin Research and Technology*, 27(2):163–177, 2021.

[63] Anna-Marie Hosking, Brandon J Coakley, Dorothy Chang, Faezeh Talebi-Liasi, Samantha Lish, Sung Won Lee, Amanda M Zong, Ian Moore, James Browning, Steven L Jacques, et al. Hyperspectral imaging in automated digital dermoscopy screening for melanoma. *Lasers in surgery and medicine*, 51(3):214–222, 2019.

[64] Education in microscopy and digital imaging, . URL https://zeiss-campus.magnet.fsu.edu/articles/lightsources/tungstenhalogen.html. Accessed: 2023-07-21.

[65] *Photographic Lenses*. United States Air Force, 1 1951. Original.

[66] Georgi T. Georgiev and James J. Butler. Long-term calibration monitoring of spectralon diffusers brdf in the air-ultraviolet. *Appl. Opt.*, 46(32):7892–7899, Nov 2007. doi: 10.1364/AO.46.007892. URL https://opg.optica.org/ao/abstract.cfm?URI=ao-46-32-7892.

[67] Saturation and blooming. URL https://www.photometrics.com/learn/imaging-topics/saturation-and-blooming. Accessed: 2023-07-21.

[68] Paul E. Tippens. *Applied Physics*. McGraw-Hill/Glencoe, 1984.

[69] Julius Adams Stratton. *Electromagnetic Theory*. McGraw-Hill, 1941.

[70] John Tyndall. Iv. on the blue colour of the sky, the polarization of skylight, and on the polarization of light by cloudy matter generally. *Proceedings of the Royal Society of London*, (17):223–233, 1869.

[71] Andrew T Young. Rayleigh scattering. *Applied optics*, 20(4):533–535, 1981.

[72] Donald F Swinehart. The beer-lambert law. *Journal of chemical education*, 39(7):333, 1962.

[73] R Alcaraz de la Osa, I Iparragirre, D Ortiz, and JM Saiz. The extended kubelka–munk theory and its application to spectroscopy. *ChemTexts*, 6:1–14, 2020.

[74] Michael L Myrick, Michael N Simcock, Megan Baranowski, Heather Brooke, Stephen L Morgan, and Jessica N McCutcheon. The kubelka-munk diffuse reflectance formula revisited. *Applied Spectroscopy Reviews*, 46(2):140–165, 2011.

[75] San Wan, R Rox Anderson, and John A Parrish. Analytical modeling for the optical properties of the skin with in vitro and in vivo applications. *Photochemistry and Photobiology*, 34(4):493–499, 1981.

[76] Scott Prahl. Optical absorption of hemoglobin. *Oregon Medical Center News*, 1999.

[77] Jane Sandby-Møller, Thomas Poulsen, and Hans Christian Wulf. Epidermal thickness at different body sites: relationship to age, gender, pigmentation, blood content, skin type and smoking habits. *Acta dermato-venereologica*, 83(6):410–413, 2003.

[78] TJS Van Mulder, M de Koeijer, H Theeten, D Willems, P Van Damme, M Demolder, G De Meyer, KCL Beyers, and V Vankerckhoven. High frequency ultrasound to assess skin thickness in healthy adults. *Vaccine*, 35(14):1810–1815, 2017.

[79] R Rox Anderson and John A Parrish. The optics of human skin. *Journal of investigative dermatology*, 77(1):13–19, 1981.

[80] MATLAB. *Image Processing Toolbox, version 11.5 (R2022a)*. The MathWorks Inc., Natick, Massachusetts, 2022.

[81] Skin optics. URL `https://omlc.org/news/jan98/skinoptics.html`. Accessed: 2023-07-21.

[82] EN Meshalkin, Vlasov IuA, TN Shishkina, GN Okuneva, and SL Pinegin. Blood oxygen saturation in various regions of the circulatory system in healthy persons. *Kardiologiia*, 22(11):45–49, 1982.

[83] Michael W Sjoding, Robert P Dickson, Theodore J Iwashyna, Steven E Gay, and Thomas S Valley. Racial bias in pulse oximetry measurement. *New England Journal of Medicine*, 383(25):2477–2478, 2020.

[84] Biointellisense adds skin-color sensitivity to pulse oximeter chips amid fda concerns over fingertip devices, . URL https://www.medtechdive.com/news/biointellisense-Medtronic-skin-color-oximeter/635570/. Accessed: 2023-07-21.